ABSTRACT

SURFACE POLARIZATION EFFECTS ON THE INFRARED ACTIVE LATTICE VIBRATIONS OF CRYSTALS

By James T. Luxon

It is widely appreciated that atomic parameters strongly affect lattice-vibration frequencies. The fact that boundary conditions--as determined by particle size and shape--strongly affect lattice-vibration frequencies in particulate polar crystals is less widely appreciated. The influence of surface polarization on lattice-vibration frequencies is investigated by examining the extent to which the infrared absorption spectra of polar crystals are influenced by particle size and shape.

The major details of the absorption spectra can be accounted for by classical electromagnetic scattering theory and a generalized Fröhlich equation, derived herein, which relates the absorption frequencies in small particles to the transverse-optical (TO) frequencies in the bulk crystal. Calculations are based on optical parameters

and TO frequencies from i.r. reflection spectra of large single crystals. The spectra of MgO, SnO_2, TiO_2, $BaTiO_3$, and $SrTiO_3$ are correlated with particle size and shape as measured by optical and electron-microscopic methods.

Fröhlich type absorptions in two distinct forms of MgO powder are found to shift with the refractive index of the surrounding medium in a predictable manner. Absorptions at 400, 550, 488, and 610 cm^{-1} in the spectra of three forms of MgO powder are accounted for on the basis of particle size and shape. In SnO_2, TO bulk-crystal frequencies of 605, 284, 243, and 465 cm^{-1} are expected to shift to 670, 330, 270, and 592 cm^{-1}; this prediction is confirmed experimentally. Similar results are found for TiO_2. In the case of $BaTiO_3$, the TO bulk-crystal frequencies of 510, 183, and 33.8 cm^{-1} are found experimentally to shift to 545, 400, and 180 cm^{-1}; the agreement with calculated frequencies is good when particle shape is considered. Similar results are obtained for $SrTiO_3$.

SURFACE POLARIZATION EFFECTS ON THE INFRARED ACTIVE LATTICE VIBRATIONS OF CRYSTALS

by

James T. Luxon

A THESIS

Submitted to
Michigan State University
in partial fulfillment of the requirements
for the degree of

DOCTOR OF PHILOSOPHY

Department of Metallurgy, Mechanics and Materials Science

1969

ACKNOWLEDGMENTS

I wish to express my sincere appreciation to Prof. Donald J. Montgomery for his patience, constant encouragement and superb counsel and guidance. I want also to express deep gratitude to Prof. Robert Summitt, with whom a close association has been very enjoyable and most rewarding. I have been extremely fortunate to have had the opportunity to work closely with two such fine people.

I would like to express thanks to all the members of the MMM department, faculty and students, who have shared their knowledge and experience with me. Particularly I want to thank Karl Puttlitz for his assistance with the electron microscope.

I wish to thank the National Science Foundation for the Science Faculty Fellowship which made it financially possible for me to pursue this work.

Finally, I want to say that my wife has made a major contribution to this work by virtue of her patience, understanding, and confidence in me.

TABLE OF CONTENTS

TABLE OF CONTENTS (cont.)

LIST OF TABLES

LIST OF FIGURES

LIST OF FIGURES (cont.)

SURFACE POLARIZATION EFFECTS ON THE INFRARED ACTIVE LATTICE VIBRATIONS OF CRYSTALS

I. INTRODUCTION

The most common approach to a discussion of crystal lattice vibrations and their interaction with electromagnetic radiation is the infinite linear diatomic chain of Born and von Karman [1, 2].

This model is a simple, but instructive, device for studying many of the phenomena associated with lattice vibrations since it is possible to write explicit equations of motion which may be solved exactly. The solutions consist of two distinct branches in the spectrum of frequency versus wave vector. The low-frequency (acoustical) branch corresponds to adjacent atoms moving in the same direction in the limit of long wavelengths. The high-frequency (optical) branch corresponds to adjacent atoms moving in opposite directions, again in the long wavelength limit.

Both branches may be further split into motions transverse and longitudinal with respect to the wave

propagation vector. The longitudinal branches generally are higher in frequency than the transverse branches as a result of polarization buildup in the longitudinal motion which effectively increases the force constants. In the case of polar lattices the transverse optical (TO) modes may be excited by a transverse electromagnetic wave, whereas the longitudinal optical (LO) modes are optically inactive. Implicit in this model is the assumption of cyclic boundary conditions which mathematically is equivalent to assuming that the lattice is infinite. Moreover, the Born-von Karman model in three dimensions commonly assumes the crystal lattice to be diatomic and of cubic symmetry with the result that in the optical branch, there will be but a single triply-degenerate TO mode and a single triply-degenerate LO mode.

The long-wavelength vibrations of the acoustical branch are equivalent to elastic waves and may be treated phenomenologically from a macroscopic point of view. The long-wavelength optical-branch vibrations, as one might expect, may be treated in a similar fashion; as is discussed later, this is the region in which first-order phonon-photon interactions occur. In the phenomenological

approach, effects of second and higher order are accounted for by the inclusion of a damping coefficient. The macroscopic approach is taken in this work, as will be seen in section II.A.

A microscopic approach to a specific crystal e.g. NaCl, leads to exactly the same conclusions as the macroscopic approach. It does give more detailed information, but generally in terms of atomic parameters that are unknown or difficult to obtain, such as effective charge and polarizability.

The macroscopic approach for a three dimensional crystal involves writing equations of motion for polarization waves for each of the normal modes predicted by group theory, and then solving these equations explicitly. In the case of large single crystals, this procedure leads to a sum-of-oscillators expression for the complex dielectric constant, which in turn enables one to compute the reflectivity or transmittance. For "small" crystals a general Fröhlich equation relating absorption frequencies and transverse-optical (TO) bulk-crystal frequencies may be deduced.

In the microscopic approach equations of motion are written for individual ions. This approach necessitates

evaluating the effective electric field, i.e., the field, E_{eff}, seen by an individual ion. This evaluation is exceedingly difficult for anything but the simplest crystals of highest symmetry. In any case the microscopic equations of motion become identical with the macroscopic equations after some manipulation [2], except that the phenomenological coefficients are identified with atomic parameters.

Previous investigators have shown that a rigorous quantum-mechanical treatment leads to the same result as the classical approach. Hence, unless there is specific interest in relating atomic parameters to lattice-vibration phenomena, the macroscopic theory is quite adequate. The earliest calculations of Born and von Karman and others assumed infinite crystal dimensions, or cyclic boundary conditions; it is important to check the validity of this assumption, and a number of investigations have been made of the magnitude of the effect of such artificial and arbitrary boundary conditions. Ledermann [17], who first looked at this problem, considered only short-range forces and concluded that, at most, the effect of free surfaces on the frequency distribution is of the order of 1/L, where L is the length of the edge of a crystal cube in units of atomic spacing. For crystals with significant long-range forces,

i.e. polar crystals, the free-surface effects are considerably greater. In the case of infrared activity, the free-surface effects are still negligible for crystals with dimensions ten times or more greater than the radiation wavelength. This, of course, is the case in most experiments on reflection from bulk crystals, and experiments on transmission of radiation incident normally on thin films.

Although there has been considerable interest in the theoretical aspects of the effect of finite boundary conditions on lattice vibrations, little work has been reported dealing with the interpretation of actual experimental data on "small" crystals. Berreman [3] has observed the LO mode of LiF by employing radiation obliquely incident on thin films. Hass [4] has deposited thin films of LiF and NaCl onto gratings in order to obtain a long, thin, cylinder-like specimen configuration. He showed that the absorption of infrared radiation varied in a predictable manner for radiation polarized parallel and perpendicular to the axes of the cylinders. Axe and Pettit [5] have interpreted the absorption spectra of UO_2 and ThO_2 in terms of the shape of particles in the powder spectrum. Summitt interpreted the absorption spectra of SnO_2 powder [6] and

fibrous SiC [7] in terms of effects of particle size and shape.

One of the earliest discussions of lattice vibrations in finite polar crystals was given by Fröhlich [8]. He related the absorption frequency of a "small" spherical, isotropic polar crystal, having a single long-wavelength transverse-optic (TO) mode, to the high-frequency and low-frequency dielectric constants and the TO frequency. Others have considered the problems of lattice dynamics of finite chains [9], thin slabs [10], cubes [11], and spheres [12], but without experimental confirmation. Many of the treatments that have been reported consider only short-range forces; such studies cannot lead to accurate quantitative predictions concerning the interaction of radiation with finite polar crystals, since here long-range forces, and perhaps retardation, must be considered. Nevertheless, there has been general agreement that additional modes (surface modes) will result from the imposition of finite boundary conditions, and that at least some of these should lead to measurable infrared absorption. Ruppin and Englman [13], recently have included in calculations the long-range forces and retardation effects, concluding that all additional modes due to finite boundary conditions automatically

are accounted for by classical scattering theory. In other words, scattering theory is a continuum approximation to the effect of a finite number of discrete modes which arise entirely from the use of finite boundary conditions. Hence, in principle it is not difficult to account for finite-crystal modes.

The considerations discussed above are not important in intramolecular vibrations, since such vibrations are relatively insensitive to other parts of the molecule or its surroundings. The spectra of such materials thus may be obtained from powdered specimens dispersed in Nujol and other media, the absorption frequencies showing little if any effect of particle size or surrounding medium. Similarly the nature of the boundary conditions for large single crystals and certain thin film or slab configurations are unimportant in that they have negligible effect on the reflection spectra or transmission spectra, respectively. Hence, when dealing with "large" crystals, although lattice vibrations of ionic crystals depend on the entire array of ions because of long-range forces, boundary conditions can be ignored or artificial ones employed. The resulting theory of photon-phonon interaction is simplified; then optical constants can be easily interpreted in terms of lattice vibrations, and

optically-active lattice-vibration frequencies can usually be accurately identified. Consequently much theoretical and experimental work has been done on thin films and large single crystals. It is not possible or always convenient to evaporate thin films of some materials, and often it is neither practical nor economical to grow suitable single crystals. It is, therefore, frequently desirable to study materials in the form of powders. Consequently, because of the scarcity of interpretive information on the spectra of powders, we have undertaken the task of developing appropriate procedures for such interpretations. We have selected well-known materials for the investigation to insure adequate data for comparative purposes. All of the materials to be considered have been studied both in powder and single-crystal form. We have contributed additional experimental information where necessary. This investigation aims to establish the usefulness of powder techniques in far infrared spectroscopy as a substitute for and to complement measurements on bulk single crystals or thin crystals or films.

The materials selected for this study were cubic MgO, Tetragonal TiO_2 (rutile), and SnO_2, and the ferroelectric perovskites $BaTiO_3$ and $SrTiO_3$. MgO was chosen because

of the ease with which powders with particles of various average grain size could be produced and because of its simple cubic symmetry. TiO_2 and SnO_2 were chosen because of their uniaxial symmetry which provides a relaxation of symmetry conditions, and serves as a check on the applicability of our methods to crystals of noncubic symmetry. $BaTiO_3$ and $SrTiO_3$ were selected chiefly because of their interest in the theory of ferroelectricity, and the possibility that work on powders of these materials might shed some light on the recurring question of the low-frequency TO mode of $BaTiO_3$.

We utilize classical electromagnetic scattering theory as applied to variously shaped particles to predict absorption frequencies. The requisite optical parameters and TO bulk-crystal frequencies are obtained from single-crystal reflection results. Also included is a derivation of a generalized Fröhlich equation which relates TO bulk-crystal frequencies and powder absorption frequencies. This equation is applied to check the consistency of scattering-theory results, and in some cases as a means of predicting absorption frequencies.

Infrared-absorption spectra have been recorded for all the materials to check and extend spectra reported in

the literature. MgO powders of various average grain size were produced, and spectra were recorded. Particle sizes and shapes have been determined by optical and electron microscopy.

II. THEORY

This investigation is concerned with the optical properties of polar crystalline materials in so far as these properties are influenced by vibrations of the atoms within the crystal lattice. Specifically, we are interested in the optical properties of crystals having at least one dimension comparable with or smaller than the wavelength of the electromagnetic radiation involved.

In a crystal containing N atoms there are N coupled oscillators; according to classical vibration theory, in the harmonic approximation, these will give rise to 3N vibration modes. Three of these modes will be pure translations, leaving 3N - 3 true vibration modes which are treated as quasiparticles (phonons) in quantum mechanics. In a polar material, changes in polarization and polarizability, which lead to infrared and Raman activity respectively, accompany some lattice vibration modes. Phonons with which electromagnetic radiation may interact (referred to as transverse optical, TO, modes in which oppositely charged ions are moving in opposite directions) typically have

frequencies of the order of 10^{13}Hz corresponding to infrared frequencies. Since the shortest wavelength that a lattice-vibration mode may have is comparable with the unit cell dimensions, the maximum value of $k = 1/\lambda$ is of the order $10^{8}cm^{-1}$. When the photon is completely absorbed in creation of the phonon, conservation of quasiparticle momentum gives

$$\underline{k}(\text{phonon}) = \underline{k}(\text{photon}) + \underline{G}$$

where $\underline{G}$ is the reciprocal lattice vector, which may be neglected for our purposes. For a frequency of the order 10^{13} Hz the photon wavevector $1/\lambda$ is of the order $10^{3}cm^{-1}$. Hence k(phonon) is of the order $10^{3}cm^{-1}$, and therefore photon-phonon interactions occur only near the center of the Brillouin zone, i.e. at long wavelengths. This is commonly referred to as the long-wavelength (k = 0) approximation. In actuality these wavelengths are long compared with unit-cell dimensions but with respect to overall crystal dimensions they may be smaller than, comparable with, or even larger than such dimensions. The latter two cases are of primary interest in this study.

Since the wavelengths in question are long compared with unit cell dimensions, the number of optical lattice-vibration modes is far less than the 3N - 3 possible

lattice vibration modes. Indeed, if we assume the infinite-wavelength approximation, equivalent atoms (i.e., those atoms generated from the unit cell by any of the space symmetry operations of the crystal lattice) will move in phase. Therefore, since equivalent atoms will have identical motions, the number of possible modes may be determined by considering the number of degrees of freedom of a single unit cell. For example, in the rutile structure the unit cell contains two TiO_2 (SnO_2) "molecules" (Cf. Fig. 1. rutile structure in sec. II.D.) of three atoms each; hence eighteen degrees of freedom and a like number of lattice modes occur. Three of these are pure translational modes corresponding to the transverse acoustical (TA) branches, and the remaining fifteen are transverse optical modes. The result of group-theoretical analysis as applied to the rutile structure will be discussed later.

Corresponding to each TO or TA mode there is a longitudinal mode, LO and LA respectively. The LO modes do not interact directly with electromagnetic radiation. The LO-mode frequencies are higher than the corresponding TO frequencies as a consequence of an effective increase in force constant caused by the build-up of polarization along the direction of propagation of the wave. For a crystal

having but a single infrared active mode, these frequencies are related by

$$\upsilon_l/\upsilon = (\epsilon_o/\epsilon_\infty)^{\frac{1}{2}}, \tag{1}$$

where υ_l and υ are respectively the LO and TO frequencies, ϵ_o is the static dielectric constant, and ϵ_∞ is the high-frequency dielectric constant. This equation, first obtained by Lyddane, Sachs, and Teller (LST) [15], has been generalized by Barker [16] for the case of lattices having more than one infrared active mode, to the form

$$\prod_j |\upsilon_{l_j}|^2/\upsilon_j^2 = \epsilon_o/\epsilon_\infty. \tag{2}$$

For non-cubic crystals this equation applies to polarization along a specific crystallographic direction. The significance of the absolute value sign on υ_{l_j} will become apparent later. Equation 2, the general LST relation applies to the most general crystal class and includes damping to account for the anharmonic effects. The derivations of Eqs. 1 and 2 are based on the assumption that the crystal lattice is large compared with the vibration wavelength. Since boundary conditions are but a small perturbation in the vibrations of large crystals, artificial boundary conditions may

be imposed at the surface of the crystal without significantly affecting the validity of these equations.

The infrared reflection spectra of bulk single crystals may be analyzed to obtain the TO-mode and LO-mode frequencies of optically-active modes. This analysis is made by obtaining a fit to the reflectivity data either by means of a sum of classical oscillators--which gives the TO modes directly, and the LO modes from zeroes of the frequency dependence of the real part of the dielectric constant ϵ'--or by the Kramers-Krönig method--which gives the TO modes in terms of the poles, and LO modes in terms of the zeroes of the ϵ' vs frequency curve. In addition, the TO mode can be measured directly from the absorption spectrum of electromagnetic radiation normally incident on a thin film.

These techniques for identifying the TO and LO frequencies all involve crystal dimensions parallel to the direction of polarization which are large compared with the wavelength, and hence requires no consideration of boundary effects.

Fröhlich has pointed out the difference between absorption frequencies of "small" polar crystals and the TO bulk-crystal frequencies. He showed that the absorption frequency υ' of a spherical specimen of a cubic polar

crystal is related to the TO frequency υ by [8]

$$\upsilon'/\upsilon = [(\epsilon_o+2)/(\epsilon_\infty+2)]^{\frac{1}{2}}, \qquad (3)$$

where ϵ_o and ϵ_∞ have the same meaning given earlier. Details of the derivation of this relation will be given subsequently when a generalized form is derived.

Berreman [3] made use of the fact that use of a crystal dimension parallel to the polarization direction smaller than the wavelength leads to absorption at a frequency different from the bulk-crystal TO frequency. He obtained absorption at a frequency equal to the bulk-crystal LO mode in LiF by reflection at non-normal incidence from a thin film deposited on a metallic substrate. Although a longitudinal phonon cannot interact with electro-magnetic radiation directly, the same longitudinal-polarization effect is achieved in the thin film as a result of charge build-up at each surface. This condition is caused by the component of the electric vector perpendicular to the film. The metallic substrate totally absorbs the component parallel to the film. Thus, the reflected radiation contains only components polarized perpendicular to the film and a definite absorption appears at a frequency equal to the LO frequency. This result is consistent with Eq. 3 in the

form stated by Hass [4] for the case of elliptical cylinders,

$$\upsilon'/\upsilon = [(\epsilon_o+e)/(\epsilon_\infty+e)]^{\frac{1}{2}}, \qquad (4)$$

where e is the ratio of the major axis a to the minor axis b of the cross-section ellipse. In the case of a thin film $e \equiv b/a = o$, and Eq. 4 reduces to

$$\upsilon'/\upsilon = (\epsilon_o/\epsilon_\infty)^{\frac{1}{2}},$$

i.e., the same form as Eq. 1, except that in this case, υ' is the absorption frequency.

Hass [4] deposited LiF and NaCl on gratings to achieve a configuration of long thin particles. With Eq. 4 he was able to explain the observed difference in frequency of the absorption bands for radiation polarized parallel and perpendicular to the grating grooves. Axe and Pettit [5] have used Eq. 3 to explain discrepancies between absorption spectra of UO_2 and ThO_2 as powders and as bulk crystals. For this purpose they modified Eq. 3 to account for the dielectric constant ϵ_m of the medium in which the powder is suspended,

$$\upsilon'/\upsilon = [(\epsilon_o+2\epsilon_m)/(\epsilon_\infty+2\epsilon_m)]^{\frac{1}{2}}. \qquad (5)$$

Summitt has applied Eq. 3 to explain the absorption spectrum of SnO_2 powder [6] and Eq. 4 to explain the absorption spectrum of fibrous SiC [7].

A. Generalized Fröhlich Equation

In this section, we derive a generalized form of Eq. 3, that is applicable to crystals of all symmetry classes, and includes damping. The development of the theory in Fröhlich's treatise [8] is followed closely, generalizations being added where needed.

In the absence of electromagnetic radiation, free charge, and conduction currents, Maxwell's equations are

$$\nabla\cdot\underline{D} = 0, \quad \nabla x\underline{E} = 0, \tag{6}$$

for polarization waves in a crystal. Since $\underline{D} = \underline{E}+4\pi\underline{P}$,

$$\nabla\cdot\underline{E} = -4\pi\nabla\cdot\underline{P} = -4\pi i\underline{k}\cdot\underline{P}, \tag{7}$$

for

$$\underline{P}\propto\underline{E}\propto\underline{D}\propto e^{i(\underline{k}\cdot\underline{r}-\omega t)}.$$

The three vectors $\underline{E}$, $\underline{D}$, and $\underline{P}$ are, therefore, parallel. For longitudinal waves $\underline{k}$ is parallel to $\underline{P}$ or $\underline{D}$, hence

$$\nabla \cdot \underline{D} = i\underline{k} \cdot \underline{D} = 0,$$

requires that $\underline{D} = 0$ which implies $\epsilon = 0$. For transverse waves $\underline{k}$ is perpendicular to $\underline{D}$ or $\underline{P}$, so that Eq. 7 along with Eq. 6 results in $\underline{E} = 0$. Thus we know that

$$\underline{D} = 0, \text{ or } \underline{E} = -4\pi \underline{P} \text{ for longitudinal waves} \quad (8)$$

$$\text{and, } \underline{E} = 0, \text{ or } \underline{D} = 4\pi \underline{P} \text{ for transverse waves.}$$

Consider now an ellipsoidal specimen whose dimensions are large compared with the lattice spacing, but small compared with the wavelength of the polarization wave. In this case the applied field causes nearly homogeneous polarization in the specimen. The total polarization is written as the sum of the optical and infrared polarization,

$$\underline{P} = \underline{P}_o + \underline{P}_{ir}. \quad (9)$$

If the ellipsoid is brought into a homogeneous field $\underline{E}_o$ parallel to any of the main axes, the field inside is uniform and is given by

$$\underline{E} = \underline{E}_o / [(\epsilon_o - 1)g + 1], \quad (10)$$

where ϵ_o is the static dielectric constant and g is a factor depending on the shape of the ellipsoid [18]. From

the fact that $\underline{P} = \underline{E}(\epsilon_o - 1)/4\pi$ we obtain

$$\underline{P} = \frac{1}{4\pi} \frac{(\epsilon_o - 1)}{(\epsilon_o - 1)g + 1} \underline{E}_o \quad \text{(Static case)}. \tag{11}$$

If $\underline{E}_o$ has a frequency which is large compared with the infrared absorption frequency but small compared with the optical resonance frequency, then $\epsilon = n^2 = \epsilon_\infty$ and the equation corresponding to Eq. 11 is,

$$\underline{P}_o = (1/4\pi)(\epsilon_\infty - 1)\underline{E}_o / [(\epsilon_\infty - 1)g + 1]. \tag{12}$$

By definition,

$$\underline{P} = (\alpha/v)\underline{E}_o, \quad \underline{P}_o = (\alpha_o/v)\underline{E}_o, \quad \underline{P}_{ir} = (\alpha_{ir}/v)\underline{E}_o, \tag{13}$$

in the static case. Here α, α_o and α_{ir} are respectively the total, optical, and infrared polarizabilities, and V is volume. Hence, from Eqs. 12, 11, and 9,

$$\alpha_{ir}/V = (1/4\pi)(\epsilon_o - \epsilon_\infty) / \left[[(\epsilon_\infty - 1)g + 1][(\epsilon_\infty + 1)g + 1] \right]. \tag{14}$$

The field inside an ellipsoid located in a uniform electric field is homogeneous and parallel to the applied field if the applied field is parallel to a principal axis of polarization [18]. If it is assumed that the crystallographic axes correspond approximately to the main axes of the ellipsoid, then the principal axes of polarization may

be taken as the ellipsoid axes. In a uniaxial crystal, such as rutile, there will then be two distinct principal polarization directions, parallel and perpendicular to the c-axis, each with a distinct set of static and high-frequency dielectric constants. For each polarization direction we can write down a scalar macroscopic equation of motion for the polarization for each allowed mode. In the case of no applied field,

$$\ddot{P}_{ir_j} + \omega_{s_j}^2 P_{ir_j} + \gamma_j P_{ir_j} = 0, \qquad (15)$$

where ω_{s_j} is the force-constant parameter (undamped oscillator frequency), γ_j is the damping coefficient, and the subscript j indicates the j-th lattice-vibration mode. Note that $\omega_{s_j}/2\pi$ would be the infrared absorption frequency in the absence of damping. It will be shown later that the effect of damping is to lower the absorption frequencies relative to the undamped case. The presence of an external time-dependent field E_o introduces a forcing term to the right side of Eq. 15,

$$(1/\omega_{s_j}^2)\ddot{P}_{ir_j} + (\gamma_j/\omega_{s_j}^2)\dot{P}_{ir_j} + P_{ir_j} = (\alpha_{ir_j}/V)E_o, \qquad (16)$$

where the coefficient of E_o has been determined by setting $\ddot{P}_{ir_j} = \dot{P}_{ir_j} = 0$ for the static case. The polarization, P_{ir_j}, and polarizabilities, α_{ir_j}, are related to the total polarization, P_{ir}, and total polarizability α_{ir}, by

$$P_{ir} = \sum_{j=1}^{N} P_{ir_j}, \tag{17}$$

and

$$\alpha_{ir} = \sum_{j=1}^{N} \alpha_{ir_j}, \tag{18}$$

where N is the number of infrared-active modes for the given crystallographic axis.

Equation 6 is identical to Fröhlich's Eq. 18.12 if it is restricted to spheres with one active mode and the damping is neglected. Equation 16 applies to an ellipsoidal specimen smaller than the wavelength in an applied external field E_o. Now consider this ellipsoid to be simply a portion of a large crystal, and the field E_o to be due to the remainder of the crystal surrounding the region in question. The field E_o will be proportional to the total polarization which now must be considered to be a superposition of the infrared polarization, P_{ir}, and an induced optical polarization, P_o, given by Eq. 12. Furthermore, the field inside

the small region, E, is composed of E_o, the contribution of the region outside the ellipsoid, and E_s, the self-field of the ellipsoid. Since $P = (1/4\pi)(\epsilon-1)\ E$ and $E = E_o/[(\epsilon-1)g+1]$ we can write

$$P = (1/4\pi)(\epsilon-1)E_o/[(\epsilon-1)g+1]. \tag{19}$$

But the field inside the ellipsoid, E, equals the external field, E_o, plus the self-field, E_s, which, with the aid of the relation between E and E_o, leads to

$$E_s = -(\epsilon-1)gE_o/[(\epsilon-1)g+1]. \tag{20}$$

Substituting Eq. 20 into Eq. 19 yields

$$E_s = -g4\pi P. \tag{21}$$

This equation for the self-field applies to a particular principal polarization direction, and g will take on different values for different axes.

Previously we established that for longitudinal waves $E = -4\pi P$ and for transverse waves $E = 0$. Therefore,

$$\begin{aligned} E_o = E+g4\pi P &= g4\pi P(\text{Transverse waves}) \\ &= -(1-g)\pi P(\text{Longitudinal waves}). \end{aligned} \tag{22}$$

Now write

$$E_o = q4\pi P = q4\pi(P_o+P_{ir}), \tag{23}$$

where q is g for transverse waves and - (1-g) for longitudinal waves. Equation 23 is now substituted into Eq. 12 to eliminate E_o. This yields

$$P_o = (\epsilon_\infty-1)qP_{ir}/[(\epsilon_\infty-1)g+1-q(\epsilon_\infty-1)]. \tag{24}$$

Introducing Eq. 24 into Eq. 23 produces the desired result for E_o:

$$E_o = q4\pi P_{ir}[(\epsilon_\infty-1)g+1]/[(\epsilon_\infty-1)(g-q)+1]. \tag{25}$$

It is now possible to write the equations of motion in the form,

$$(1/\omega_{s_j}^2)\ddot{P}_{ir_j}+(\gamma_j/\omega_{s_j}^2)\dot{P}_{ir_j}+P_{ir_j}=(\alpha_{ir_j}/v)\frac{q4\pi P_{ir}[(\epsilon_\infty-1)g+1]}{(\epsilon_\infty-1)(g-q)+1} \tag{26}$$

Equation 26 represents the equations of motion of the polarization waves for a specimen which is large compared with the wavelength. Solutions of these equations yield the TO bulk-crystal frequencies for q = g, and the LO frequencies for q = -(1-g), in terms of the force constant parameters ω_{s_j} of specimens which are small compared with the wavelength.

Since $\alpha_{ir} = \sum_{j=1}^{N} \alpha_{ir_j}$, the coefficient of P_{ir} on the right side of Eq. 25 can be replaced by C_j, where

$$C = \sum_{j=1}^{N} C_j = (\alpha_{ir}/v)\, q4\pi[(\epsilon_\infty - 1)g + 1]/\left[[(\epsilon_\infty - 1)(g-q)+1]\right] = q(\epsilon_o - \epsilon_\infty)/\left[[(\epsilon_o - 1)g+1][(\epsilon_\infty - 1)(g-q)+1]\right]. \quad (27)$$

Solutions of the form $P_{ir_j} = P_j e^{i(kx-\omega t)}$ are substituted into Eq. 26 yielding

(28)

$$-(\omega^2/\omega_{s_j}^2)P_1 + (i\gamma_1\omega/\omega_{s_1}^2)P_1 + P_1(1-C_1) + C_1(P_2+P_3+\ldots+P_N) = 0$$

$$-(\omega^2/\omega_{s_2}^2)P_2 + (i\gamma_2\omega/\omega_{s_2}^2)P_2 + P_2(1-C_2) + C_2(P_1+P_3+\ldots+P_{N-1}) = 0$$

$$\vdots$$

$$-(\omega^2/\omega_{s_N}^2)P_N + (i\gamma_N\omega_{s_N})P_N + P_N(1-C_N) + C_N(P_1+P_2+\ldots+P_{N-1}) = 0$$

Equations 28 form a set of N linear homogeneous equations in the N polarization amplitudes for nontrivial solutions to exist. The determinant of the coefficients must vanish. With $A_1 = -\omega^2/\omega_{s_1}^2 + i\gamma_1\omega/\omega_{s_1}$, and so forth, the determinant becomes

$$\begin{vmatrix} A_1+1-C_1 & -C_1 & -C_1 \ldots -C_1 \\ -C_2 & A_2+1-C_2 & -C_2 \ldots -C_2 \\ \cdot & & \\ \cdot & & \\ \cdot & & \\ -C_N & -C_N & -C_N \ldots A_N+1-C_N \end{vmatrix} = 0. \tag{29}$$

By subtracting column one from every other column this determinant may be put in the form,

$$\begin{vmatrix} (A_1+1)-C_1 & -(A_1+1) & -(A_1+1) \ldots -(A_1+1) \\ -C_2 & -(A_2+1) & 0 \ldots 0 \\ -C_3 & 0 & (A_3+1) \ldots 0 \\ \cdot & & \\ \cdot & & \\ \cdot & & \\ -C_N & 0 & 0 \ldots (A_N+1) \end{vmatrix} = 0, \tag{30}$$

which upon evaluation leads to the result,

$$
\begin{aligned}
&[(A_1+1)-C_1]\,[(A_2+1)(A_3+1) \quad \ldots \quad (A_N+1)] \\
&\quad +C_2\,[-(A_1+1)(A_3+1) \quad \ldots \quad (A_N+1)] \\
&\quad -C_3\,[(A_1+1)(A_2+2)(A_4+1) \quad \ldots \quad (A_N+1)] \\
&\quad +C_3\,[-A_1+1)(A_2+1)(A_3+1)(A_5+1) \quad \ldots \quad (A_N+1)] \\
&\quad \cdot \\
&\quad \cdot \qquad\qquad\qquad\qquad\qquad\qquad\qquad\qquad\qquad\qquad (31) \\
&\quad \cdot \\
&\quad -C_n\,[(A_1+1)\ldots(A_{n-1}+1)(A_{n+1}+1)\ldots \quad (A_N+1)] \\
&\quad \cdot \\
&\quad \cdot \\
&\quad \cdot \\
&\quad -C_N\,[(A_1+1)(A_2+1) \quad \ldots \quad (A_{N-1}+1)] = 0.
\end{aligned}
$$

Carrying out the multiplication for a given value of N gives an equation with the leading term $(-1)^N\,\omega^{2N}$ and a constant term $\omega_{s1}^2\,\omega_{s2}^2\,\omega_{s3}^2 \ldots \omega_{sN}^2(1 - C_1 - C_2 - \ldots - C_N)$. The coefficients of the even-power terms are real, whereas the coefficients of the odd-power terms are imaginary. Consequently if ω_j is a solution, then $-\omega_j^*$ is also a solution. For an equation of this form the product of the solutions must equal $(-1)^N$ times the constant term. Hence,

$$\prod_j |\omega_j|^2 = \prod_j \omega_{s_j}^2 (1-C), \tag{32}$$

where $(-1)^N$ has been cancelled on each side, or

$$\prod_j \omega_{s_j}^2 / |\omega_j|^2 = 1/(1-C). \tag{33}$$

With the aid of Eq. 27 we get

$$\prod_j \omega_{s_j}^2 / |\omega_j|^2 = \frac{[(\epsilon_o-1)g+1][(\epsilon_\infty-1)(g-q)+1]}{[(\epsilon_o-1)g+1][(\epsilon_\infty-1)(g-q)-1]-g(\epsilon_o-\epsilon_\infty)}. \tag{34}$$

For the TO mode for spheres $g = q = 1/3$ and Eq. 34 becomes

$$\prod_j \omega_{s_j}^2 / |\omega_j|^2 = (\epsilon_o+2)/(\epsilon_\infty+2), \tag{35}$$

which if damping is neglected for a single mode reduces to Fröhlich's equation. In general the TO bulk-crystal modes are given by

$$\prod_j \omega_{s_j}^2 / |\omega_j^{TO}|^2 = [(\epsilon_o-1)g+1]/[(\epsilon_\infty-1)g+1] \tag{36}$$

and the LO modes by,

$$\prod_j \omega_{s_j}^2 / |\omega_j^{LO}|^2 = \left[[(\epsilon_o-1)g+1]/[(\epsilon_\infty-1)g+1]\right](\epsilon_\infty/\epsilon_o). \tag{37}$$

Dividing Eq. 36 by Eq. 37 leads to

$$\prod_j |\omega_j^{LO}| / |\omega_j^{TO}| = \epsilon_o/\epsilon_\infty, \tag{38}$$

which gives the LO modes in terms of the TO modes independent of shape, as would be expected.

Equation 36 is the desired generalized Fröhlich equation, and Eq. 38 is the generalized LST relation. Barker [16] has pointed out that the transverse-phonon frequencies, defined as poles of the dielectric constant, are related to the undamped bulk-crystal-oscillator frequencies by

$$\omega_j^{TO} = \pm \sqrt{\omega_j^2 - \gamma_j^2/4} + i\gamma_j/2. \tag{39}$$

Noting that $|\omega_j^{TO}| = \omega_j^2$ Eq. 38 can be written,

$$\prod_j |\omega_j^{LO}|^2 / \omega_j^2 = \epsilon_o/\epsilon_\infty, \tag{40}$$

and Eq. 36 becomes

$$\prod_j \omega_{s_j}^2 / \omega_j^2 = [(\epsilon_o - 1)g + \epsilon_m] / [(\epsilon_\infty - 1)g + \epsilon_m], \tag{41}$$

where ϵ_m, the dielectric constant of the medium, has been included. Equation 40, the general LST relation, agrees with Barker's result derived from a purely macroscopic point of view, as we have done here, but without introduction of the small-particle absorption frequencies, ω_{s_j}.

In actuality the ω_{s_j}'s introduced here, aside from a factor of 2π, are the undamped small-particle absorption frequencies (force-constant parameters). Equation 41 relates the ω_{s_j}'s to the bulk-crystal undamped TO frequencies (force-constant parameters). The actual absorption frequency for the bulk crystal is given by the real part of Eq. 39. Unless excessive damping occurs, however, as apparently is the case in the "soft" optic mode of $BaTiO_3$, the damped and undamped frequencies are essentially the same. With the exception of $BaTiO_3$, damping in the materials considered in this work is not sufficient to cause a difference of more than one or two wavenumbers between these two frequencies.

B. Electromagnetic Scattering Theory

Classical electromagnetic scattering theory allows us to compute the absorption frequencies of powdered polar crystalline materials from the complex refractive index, $m = n - ik$. The complex refractive index may be determined from experimental reflectance data by use of Kramers-Krönig analysis or classical dispersion analysis. All of the refractive-index data used in this study has been computed by the latter method.

In classical dispersion analysis, the complex dielectric constant is written in terms of a sum of harmonic oscillators

$$\epsilon = \epsilon' + i\epsilon'' = \epsilon_\infty + \sum_{j=1}^{N} \frac{4\pi\rho_j \upsilon_j^2}{\upsilon_j^2 - \upsilon^2 + i\gamma_j \upsilon \upsilon_j}, \qquad (42)$$

for polarization parallel to a given crystallographic axis. In this equation ϵ_∞ is the high-frequency electronic contribution to the dielectric constant, γ_j is the dimensionless damping coefficient, $4\pi\rho_j$ is the dimensionless mode strength, and υ_j is the j-th mode oscillator frequency. The damping, γ_j, takes into account anharmonic effects which cause line broadening, and thus is related to the line width of the j'th oscillator mode. The mode strength, $4\pi\rho_j$, is related to the effective charge and polarization of the j'th mode. An equation identical to Eq. 42 applies to each unique axis of the crystal, e.g., rutile requires three oscillators perpendicular to the c-axis, and one oscillator parallel to it.

The parameters, υ_j, γ_j, and $4\pi\rho_j$ are adjusted by successive approximation to give the best fit to the experimental reflectance data through the relation

$$R = \left|(1 - \sqrt{\epsilon})/(1 + \sqrt{\epsilon})\right|^2, \tag{43}$$

where

$$\epsilon' = n^2 - k^2 = \epsilon_\infty + \sum_j \frac{4\pi\rho_j \upsilon_j (\upsilon_j^2 - \upsilon^2)}{(\upsilon_j^2 - \upsilon^2)^2 + \gamma_j \upsilon_j^2 \upsilon^2}, \tag{44}$$

and

$$\epsilon'' = 2nk = \sum_j \frac{4\pi\rho_j \gamma_j \upsilon_j \upsilon}{(\upsilon_j^2 - \upsilon^2)^2 + \gamma_j^2 \upsilon^2} . \tag{45}$$

In the case of $BaTiO_3$ and $SrTiO_3$, Barker and Hopfield [19], by use of a coupled-oscillator model, were able to obtain a better fit to the reflectivity data. The dielectric constant for a three-oscillator model with two interacting oscillators is given by

$$\epsilon = \epsilon_\infty + \epsilon_1 + \epsilon_2 + \epsilon_3, \tag{46}$$

where

$$\epsilon_1 = \frac{4\pi z_1^2 + i4\pi z_1 z_2 \upsilon\gamma_{12}/[\upsilon_2^2 - \upsilon^2 + i\upsilon(\gamma_2 + \gamma_{12})]}{\upsilon_1^2 - \upsilon^2 + i\upsilon(\gamma_1 + \gamma_{12}) + \upsilon^2\gamma_{12}/[\upsilon_2^2 - \upsilon^2 + i\upsilon(\gamma_2 + \gamma_{12})]}, \tag{47}$$

and ϵ_2 is given by cyclic permutation of the subscripts in Eq. 47. The remaining dielectric term, ϵ_3, is given by

$$\epsilon_3 = 4\pi z_3^2/(\upsilon_3^2 - \upsilon^2 + i\upsilon\gamma_3) . \tag{48}$$

In Eqs. 47 and 48, $4\pi z_1^2/\upsilon_1^2$ is the same as $4\pi\rho_1$, and γ_1/υ_1 the same as γ_1, in our previous notation. The interaction damping between oscillators 1 and 2 is accounted for by γ_{12}. The reflectance and the complex refractive index are still related to ϵ by Eq. 43, $\epsilon'=n^2-k^2$ and $\epsilon''=2nk$, so that the procedure for determining the absorption frequencies of the powders remains unchanged.

We have mentioned that Barker [16] has pointed out that the transverse-phonon frequency for independent, damped harmonic oscillators is given by

$$\upsilon_j^{TO} = i\gamma_j/2 \pm \sqrt{-\gamma_j^2/4 + \upsilon_j^2} \quad . \tag{49}$$

The absolute square of the complex transverse phonon frequency υ_{p_j}, equals the square of the undamped oscillator frequency υ_j; thus,

$$|\upsilon_{p_j}^{TO}|^2 = \upsilon_j^2 \quad , \tag{50}$$

which justifies the use of the undamped frequencies in the general Fröhlich equation (Eq. 41) as well as the general LST relation. The actual frequency at which the phonon-photon interaction occurs in the case of absorption in thin films, thin crystal slabs, or in Raman scattering is

$\sqrt{-\gamma_j^2/4 + \upsilon_j^2}$, which is within one percent of υ_j for a value of $\gamma_j/\upsilon_j = 0.3$. Consequently, no significant shift should appear unless extreme damping occurs.

To estimate the effect of damping in the case of coupled oscillators, we examine the poles of the dielectric constant which are given by

$$\upsilon^4+\upsilon^3(-i)(\gamma_1+\gamma_2+2\gamma_{12})+\upsilon^2\Big[-\upsilon_2^2-\upsilon_1^2-(\gamma_2+\gamma_{12})\cdot (\gamma_1+\gamma_{12})+\gamma_{12}^2\Big]+\upsilon(i)\Big[\upsilon_2^2(\gamma_1+\gamma_{12})+\upsilon_1^2\cdot (\gamma_2+\gamma_{12})\Big] + \upsilon_2^2\upsilon_1^2 = 0. \tag{51}$$

By virtue of the form of the coefficients, if υ_{p_i} is a solution then $-\upsilon_{p_i}^*$ is a solution; thus,

$$|\upsilon_{p_1}|^2|\upsilon_{p_2}|^2 = \upsilon_1^2\,\upsilon_2^2 , \tag{52}$$

and

$$\upsilon_{p_1} - \upsilon_{p_1}^* + \upsilon_{p_2} - \upsilon_{p_2}^* = \gamma_1 + \gamma_2 + 2\gamma_{12} . \tag{53}$$

Equations 52 and 53 are based on the fact that the sum of all possible products of the roots of a polynomial taken k at a time equals $(-1^k a_k/a_o)$ for a polynomial of the form,

$$a_o x^n+a_1 x^{n-1}+a_2 x^{n-2}+ \ldots + a_n = 0.$$

Upon writing $\upsilon_{p_1} = \upsilon'_{p_1} + i\upsilon''_{p_1}$, etc., Eq. 53 leads to

$$\upsilon''_{p_1} + \upsilon''_{p_2} = \tfrac{1}{2}(\gamma_1+\gamma_2+2\gamma_{12}) . \tag{54}$$

If we guess that

$$\upsilon''_{p_1} = \tfrac{1}{2}(\gamma_1+\gamma_{12}) \quad \text{and} \quad \upsilon''_{p_2} = \tfrac{1}{2}(\gamma_2+\gamma_{12}) \tag{55}$$

then Eq. 52 leads to

$$\upsilon_{p_1} = \pm \sqrt{-\tfrac{1}{4}(\gamma_1+\gamma_{12})^2+\upsilon^2} + \tfrac{1}{2}i(\gamma_1+\gamma_{12}) ,$$

and (56)

$$\upsilon_{p_2} = \pm \sqrt{-\tfrac{1}{4}(\gamma_2+\gamma_{12})^2+\upsilon_2^2} + \tfrac{1}{2}i(\gamma_2+\gamma_{12}) .$$

That these are the correct roots may be checked by applying the root-coefficient relation to the coefficients of υ^2 and υ. It may be observed that in the event that the analysis requires coupled harmonic oscillators, the damped and undamped frequencies differ only slightly except in the case of extreme damping, as in the case of independent damped oscillators.

Once the complex refractive index has been computed as a function of frequency, the electromagnetic extinction

cross-section may be determined. The extinction cross-section, $C^{(ext)}$, relates to the energy loss from a radiation beam due to a single particle, and may be written as the sum of a pure scattering cross-section, $C^{(sca)}$, and a pure absorption cross-section, $C^{(abs)}$. For spheres of arbitrary size, $C^{(ext)}$ may be written as a series,

$$C^{(ext)} = -\pi a^2 \mathrm{Im}\left[4x\frac{m^2-1}{m^2+2} + \frac{4}{15}x\left(\frac{m^2-1}{m^2+2}\right)^2\frac{m^4+27m^2+38}{2m^2+3} + \ldots\right] + x^4\mathrm{Re}\left[\frac{8}{3}\left(\frac{m^2-1}{m^2+2}\right)^2\left[1 + \frac{6}{5}\frac{m^2-1}{m^2+2}x^2 + \ldots\right]\right] \quad (57)$$

where $x \equiv 2\pi a/\lambda$, $m \equiv n - ik$, and a is the particle radius [20]. For sufficiently small arbitrarily-shaped particles, $C^{(ext)}$ and $C^{(abs)}$ may be expressed approximately as

$$C_j^{(sca)} = \frac{8}{3}\pi k^4 |\alpha_j|^2 , \quad (58)$$

and

$$C_j^{(abs)} = -4\pi k \mathrm{Im}(\alpha_j) ,$$

where $k = 2\pi/\lambda$ and the polarizability, α_j, is given by

$$V/4\pi\alpha_j = g_j + 1/(m^2-1) . \quad (59)$$

The subscript j in Equations 58 and 59 refers to the particular direction of polarization. In the case of a

uniaxial crystal, separate scattering cross-sections must be computed for polarization parallel and perpendicular to the c-axis. In Eq. 59 V is the particle volume and g_j has the same identification as previously, i.e., it is a shape factor which allows us to consider the more general case of ellipsoidal particles. In this work, calculations for various shape factors have been made, and consequently Eqs. 58 primarily were employed. An additional term in the series expansion for spheres was included in some calculations, however, to provide a basis for judging the effect of particle size.

To determine the transmittance of a powder consisting of particles of a uniaxial crystal, the incident radiation intensity is averaged over all crystallographic orientations. The particles may be assumed to be randomly oriented in the absence of any force that might be present to align them. The desired average is determined by finding the average of the square of the electric-vector projection on a particular axis for all possible orientations of the electric vector $\underline{E}$. Since the average squared projection for each of three mutually orthogonal axes must be equal ($\overline{E}_x^2 = \overline{E}_y^2 = \overline{E}_z^2$), and the sums of the squares must equal

the square of the electric vector ($\bar{E}_x^2 + \bar{E}_y^2 + \bar{E}_z^2 = \bar{E}^2$), the average squared projection equals $\bar{E}^2/3$. On the average, then, each axis will see one-third the incident energy, and the effective cross-section, C(eff) should be written as a sum of the cross-sections for polarization along the particular axes. Hence,

$$C(\text{eff}) = \frac{1}{3} C_x^{(\text{ext})} + \frac{1}{3} C_y^{(\text{ext})} + \frac{1}{3} C_z^{(\text{ext})}$$
$$= \frac{2}{3} C_x^{(\text{ext})} + \frac{1}{3} C_z^{(\text{ext})} , \qquad (60)$$

for a uniaxial crystal.

The transmittance may then be written as

$$T = 1 - (N/3)[2C_x^{(\text{ext})} + C_z^{(\text{ext})}] \qquad (61)$$

where $C_x^{(\text{ext})}$ applies to the $E \perp C$ direction of polarization, $C_z^{(\text{ext})}$ applies to the $E \parallel C$ direction of polarization, and N is the total number of particles in the beam. Multiple scattering and interaction have been neglected.

C. Surface Modes

According to the work of Rupin and Englman [13], the calculations of $C^{(\text{ext})}$ includes contributions to the absorption

spectrum by surface modes arising as a consequence of long-range forces and finite crystal dimensions. Their treatment of spheres includes electro-magnetic retardation, but neglects changes in short-range forces near the surface. Except in the case of particles whose dimensions are of the order of ten to one hundred unit cells, the changes in short-range forces would be expected to be minor compared with the long-range electromagnetic force. This assertion is based on the fact that surface-tension effects and changes in mean-square-displacements near the surface of crystals apparently vanish within five to ten atomic layers [21, 22]. This contention leads us to conclude that the presence of a free surface has no effect on atoms much more than five to ten unit cells from the surface, except for the case of long-range polarization effects.

Since $C^{(ext)}$ accounts for all of the polarization-type surface modes, it is not necessary to consider surface modes directly. It is useful, however, to compare the prediction of Ruppin and Englman with our scattering-theory computations, and to examine explicitly the limiting frequencies at which surface modes may contribute to absorption. Ruppin and Englman [13] have found that the

electric-type modes (which they refer to as surface modes, essentially arising from long-range forces) occur at frequencies given by

$$\epsilon \{k^{o}Rn_{\ell}(k^{o}R)\}' j_{\ell}(k^{i}R) = \{k^{i}Rj_{\ell}(k^{i}R)\}' n_{\ell}(k^{o}R) \quad (62)$$

and the magnetic-type modes (due to short-range forces) are given by

$$j_{\ell}(k^{i}R)\{k^{o}Rn_{\ell}(k^{o}R)\}' = n_{\ell}(k^{o}R)\{k^{i}Rj_{\ell}(k^{i}R)\}'. \quad (63)$$

In Eqs. 62 and 63 j_{ℓ} and n_{ℓ} are respectively Bessel and Neumann functions, k^{i} is $\sqrt{\epsilon}\ 2\pi\upsilon/c$, k^{o} is $2\pi\upsilon/C$, and R is the particle radius. The prime indicates differentiation with respect to the argument of the Bessel or Neumann function. For kR much less than 1.0, n_{ℓ} approximates $(kR)^{-(\ell+1)}$, and $j_{\ell}(kR)$ approximates $(kR)^{\ell}$. These approximations lead to

$$\epsilon = -(\ell+1)/\ell, \quad \ell = 1,2,3 \ldots \quad (64)$$

for the electric modes; the contribution from the magnetic modes vanishes since, in this approximation, the number of such modes--proportional to the volume--approaches zero. For a one-oscillator model having a dielectric constant of the form

$$\epsilon = \epsilon_{\infty} + (\epsilon_{o}-\epsilon_{\infty})/(1-\upsilon^{2}/\upsilon_{t}^{2}) , \quad (65)$$

Eq. 64 becomes,

$$\upsilon_s/\upsilon_t = [\epsilon_o+\epsilon(\ell+1)/\ell]/[\epsilon_\infty+\epsilon_m(\ell+1)/\ell] \ , \qquad (66)$$

where ϵ_m has been included to account for the refractive index of the medium surrounding the particles. For $\ell = 1$ Eq. 66 reduces to the Fröhlich relation, and for $\ell = \infty$ we obtain the limit to which the surface-mode frequencies converge:

$$\upsilon_s/\upsilon_t = (\epsilon_o+\epsilon_m)/(\epsilon_\infty+\epsilon_m) \ . \qquad (67)$$

The total number of modes is not infinite, but is proportional to the surface area. Equation 66 suggests that absorption lines should be asymmetrical, i.e., skewed toward higher frequencies. According to Ruppin and Englman, this effect is more pronounced in larger particles, which is consistent with our scattering calculations based on the complex refractive index.

D. Vibration Analysis

This section presents a brief statement of the results of standard group-theoretical analysis as applied to crystals to determine their first-order, long-wavelength

optical vibration modes. The case of MgO is excluded from this discussion since only one such mode in this structure (the rock-salt structure, two interpenetrating face-centered cubic lattices) gives rise to a change in polarization. This mode is a vibration in which the two lattices (Mg^{2+} and O^{2-}) are each vibrating as a whole, but in opposite directions.

The number and type of fundamental TO modes for a given crystal structure may be determined by the methods of group-theoretical analysis. Application of these methods to the crystal space group allows the prediction of the symmetry species of each of the allowable modes, and quantum-mechanical selection rules predict which modes are infrared or Raman active. Symmetry coordinates may be computed in a straightforward manner. The symmetry coordinates provide a graphic description of the motions of the atoms in the various modes. In the absence of degeneracy the symmetry modes are normal modes.

(i) SnO_2 and TiO_2

In the case of SnO_2 and TiO_2, which have tetragonal structure, D_{4h}^{14}, group theory leads to the irreducible representation [24],

$$\Gamma = A_{1g}+A_{2g}+A_{2u}+B_{1g}+B_{2g}+E_g+2B_{1u}+3E_u$$

The modes of symmetry species A_{2u} and E_u are infrared active. The symmetry coordinates of the A_{2u} and three doubly-degenerate E_u modes are reproduced in Fig. 1

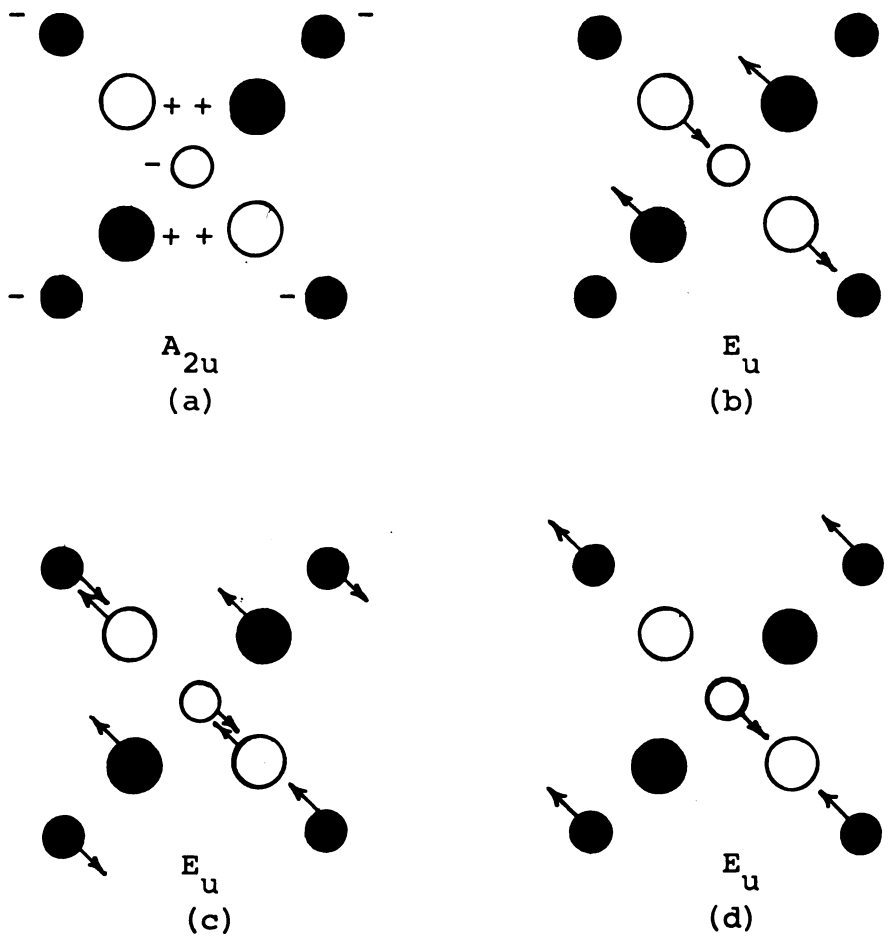

Figure 1.--Infrared-active symmetry modes of the rutile structure.

Each diagram in Fig. 1 is a view along the c-axis of the rutile unit cell. The small circles represent Ti^{4+} or Sn^{4+} ions, and the large circles represent O^{2-} ions.

Dark ions are in the top plane of the unit cell. Light circles are in the mid-plane, + and - represent displacement in the positive and negative z- direction (c-axis).

It is clear from the symmetry coordinates that the A_{2u} mode is active for infrared radiation polarized parallel to the c-axis, and that the three E_u modes are active in radiation polarized perpendicular to the c-axis.

(ii) $BaTiO_3$ and $SrTiO_3$

The perovskites, $BaTiO_3$ and $SrTiO_3$, have O_h symmetry in the cubic phase, and C_{4v} symmetry in the tetragonal (ferroelectric) phase. The ferroelectric transition temperatures for $BaTiO_3$ and $SrTiO_3$ are, respectively, 133°C [23] and -163°C [34]. Consequently at room temperature $BaTiO_3$ is tetragonal and $SrTiO_3$ is cubic. All of the measurements of this study were made at room temperature.

The unit cell of this structure includes five atoms and hence there are 15 degrees of freedom. For O_h symmetry these divide into representations $4F_{1u} + F_{2u}$ [23] where in each F mode is triply degenerate. One of the modes of F_{1u} symmetry is a pure translational mode (acoustical branch), and the remaining three are infrared active. In the tetragonal phase each of the F_{1u} modes splits into modes of symmetry species $A_1 + E$, and the F_{2u} mode splits into $B_1 + E$.

Modes of symmetry species E are doubly degenerate. Thus the $O_h \longrightarrow C_{4v}$ transition may be represented as,

$$3\ F_{1u} + 1F_{2u} \longrightarrow 3A_1 + 1B_1 + 4E.$$

The A_1 modes are infrared active for polarization parallel to the c-axis, and the E modes are infrared active for polarization perpendicular to the c-axis. Since the splitting of the F_{1u} and F_{2u} modes is not expected to be very great, we do not distinguish between O_h and C_{4v} symmetry in this work. Separation of these modes in infrared absorption spectra of these powders was not possible because of extensive broadening of the bands due to variations in particle shape.

III. APPARATUS AND SAMPLE PREPARATION

The spectra obtained by this writer were recorded on two instruments to cover a frequency range from 167 cm^{-1} to 800 cm^{-1}. In the range from 167 cm^{-1} to 667 cm^{-1} a Perkin-Elmer Model 301 double-beam spectrophotometer was used. To extend certain spectra to 800 cm^{-1}, a Perkin-Elmer Model 137 double-beam potassium-bromide prism spectrophotometer was used. Many of the MgO spectra reported herein had been recorded earlier by D. J. Montgomery and K. F. Yeung on the Model 137 spectrophotometer mentioned above and on a Perkin-Elmer Model 21 spectrophotometer equipped with a cesium bromide prism to cover the region 270-1000 cm^{-1}.

The Model 301 spectrophotometer is a double-beam grating instrument which contains a combination of variable-transmission filters, choppers, and reflection elements to isolate a narrow band of the electromagnetic spectrum and to decrease the influence of stray light. The radiation source in this work was a globar. A Golay detector served to determine the intensity of the transmitted beams and the

ratio of the two signals is plotted on a strip-chart recorder. Slit width is varied automatically to maintain a nearly constant energy level over the entire frequency range. The overall performance is very good, with a signal-to-noise ratio of better than 25 to 1, and scattered light less than 2%. The resolution is 0.7 cm^{-1} at 214 cm^{-1}. Spectra could be reproduced within less than 1.0 cm^{-1}.

Possible difficulties may occur from water-vapor absorption below 400 cm^{-1}, and excessive absorption by the polyethylene windows above 600 cm^{-1}. The water vapor problem was minimized by flushing with dry nitrogen. Results obtained with polyethylene windows were checked with KBr windows to ascertain the effect of the loss of energy. No significant difference was discernible in the spectra run with polyethylene and KBr windows in the 400 to 667 cm^{-1} region.

Three instrument change points occur in the 667 cm^{-1} to 167 cm^{-1} region. Between 667 cm^{-1} and 320 cm^{-1} a filter change is required; the reproducibility at this filter change is excellent. At 320 cm^{-1} the choppers must be changed from opaque to KBr; the reproducibility at this point is satisfactory. A filter change at 210 cm^{-1} is a

little more troublesome for some undetermined reason, but no difficulty has been encountered in interpreting the spectra. If absolute intensities were a matter of concern, we should have a problem here.

The Perkin-Elmer Model 137 spectrophotometer, though a much less sophisticated instrument than the Model 301, yields excellent reproducibility of spectra. Repeated runs give maximum-absorption wavelengths within less than 0.1μ. The source of radiation in this instrument is a globar, and the detector is a thermocouple. The spectra are recorded continuously on a drum chart. Slit width is controlled manually.

All powder samples studied in this work were prepared as Nujol mulls, with the exception in some cases where smoke was fumed directly onto polyethylene or KBr plates. Since absolute intensities were not of particular interest in this work, most samples were prepared without weighing the oil or powder. A sample of a few milligrams of powder was added to five to ten drops of Nujol in a plastic vial containing a plastic ball of diameter slightly less than that of the vial. The mixture was then agitated by means of a Wig-L-Bug vibrator. This operation broke up loosely aggregated particles and dispersed them throughout

the Nujol. The mull was then placed between polyethylene or KBr plates, the choice depending on the spectral range. Variations in powder concentration affected only intensities, not absorption frequencies. A pair of plates was always placed in the reference beam to compensate for extinction by the plates themselves. In the case of KBr plates, compensation is excellent. Differences in thickness of the polyethylene plates makes compensation less complete but nevertheless satisfactory.

A large fraction of the MgO data quoted herein were recorded previously by D. J. Montgomery and K. F. Yeung who used a Perkin-Elmer Model 21 spectrophotometer equipped with a cesium bromide prism to cover the region 270-1000 cm^{-1}, as well as the previously-mentioned Perkin-Elmer Model 137 spectrophotometer. The quality of the Model 21 spectra exceeds that of the Model 137, but the data are comparable. The samples were prepared in the form of alkali halide pressed pellets, and MgO in the form of smoke deposited directly on KBr plates.

Particle size and shape were observed in this work by both the optical microscope and the electron microscope. Optical observations were made with a Unitron MPS microscope equipped with a Cooke AEI image-splitting eyepiece.

This eyepiece consists of a system of prisms linked to a micrometer screw by which the angular relation between the prisms may be varied. When the prism faces are parallel the images are superimposed. When the micrometer screw is turned the images shear across each other. Filters are inserted to make one image appear red and the other green. The amount of shear required to make the edges of the images touch is equal to the dimension of the object. The micrometer is calibrated with a substage micrometer. Measuring accuracy for the image-splitting eyepiece is 0.325μ for a 40X objective lens.

Electron micrographs were obtained on a Hitachi HU-11-A electron microscope. Since great precision in particle-size measurement was not necessary magnification was determined from charts of magnification versus lens current for various pole-piece settings which are supplied by the manufacturer. The negative images are recorded on Kodak electron-image plates, and additional magnification may be achieved when these negatives are printed.

Support films for the powder particles were made by coating 400-mesh copper grids with formvar or carbon. The carbon-coated grids were prepared by vacuum-depositing carbon vapor on a microscope slide. With a scribe the

film is cut into squares approximately 3 mm on a side. The film is then floated off the slide by slowly lowering the slide into distilled water with an angle of about 30° between the slide and water. The squares of carbon film are picked up on the grids with a pair of pointed tweezers to hold the grid, and bringing it up underneath the film to lift the square clear of the water. The coated grids are then stored by sticking them to two-sided plastic tape which has been placed on the edge of a microscope slide.

The formvar film was prepared by placing a few drops of 0.1% solution of formvar in ethylene dichloride on a clean microscope slide and dragging a second slide across it to achieve a thin coating. After the ethylene dichloride evaporates, the film is cut and placed on the grids in the same manner as the carbon film.

The powder particles were deposited on the film-covered grids by dispersing a minute quantity of the powder in distilled water. A specimen is prepared by placing a drop of this mixture on a coated grid. The powder particles stick to the film after the water evaporates. Specimens of MgO smoke particles were prepared by the previous method and also by fuming the smoke particles directly onto the coated grids.

IV. EXPERIMENTAL DATA

This section contains pertinent infrared spectra obtained from the literature as well as those recorded by this writer and by Montgomery and co-workers. The section is divided into three main parts, according to crystal structure: the first deals with MgO (rock-salt structure), the second with TiO_2 and SnO_2 (rutile structure), and the third with $BaTiO_3$ and $SrTiO_3$ (perovskite structure). Each part describes the salient features of the various spectra, and gives the results of optical-microscope and electron-microscope investigations.

A. Magnesium Oxide

Three forms of particulate MgO were studied in this investigation. The first, to be referred to as MgO(1), consisted of powders obtained from various commercial sources, such as K and K Laboratories and Harshaw Chemical Company. Although these powders varied somewhat in purity, all were 0.99+ pure and no effects were observed in the

infrared absorption spectrum which could be attributed to impurities.

The optical microscope shows that MgO(1) powder contains particles as large as several microns in diameter. After dry grinding in the Wig-L-Bug, the large particles break up into smaller ones, of diameter 0.5μ or less, the proportion of larger particles remaining negligible. Grinding in Nujol has essentially the same effect. Figure 2 is an electron micrograph of a commercial MgO powder. This photograph confirms the optical-microscopic findings and enables a more precise estimate to be made of particle size and shape. It can be seen in this micrograph that the average particle size is indeed less than 0.5μ, and that the shape is fairly irregular though devoid of flat faces or sharp corners and edges.

In Fig. 3 are illustrated two typical absorption spectra obtained by Montgomery and co-workers. One spectrum is of MgO dispersed in KBr and pressed into a pellet, the other is of MgO dispersed in CsI and pressed into a pellet. There are two strong, broad absorption bands centered near 550 cm^{-1}. The maximum-absorption frequencies are slightly different for the KBr and CsI pellets. Figure 4 is a plot of observed frequency of maximum absorption

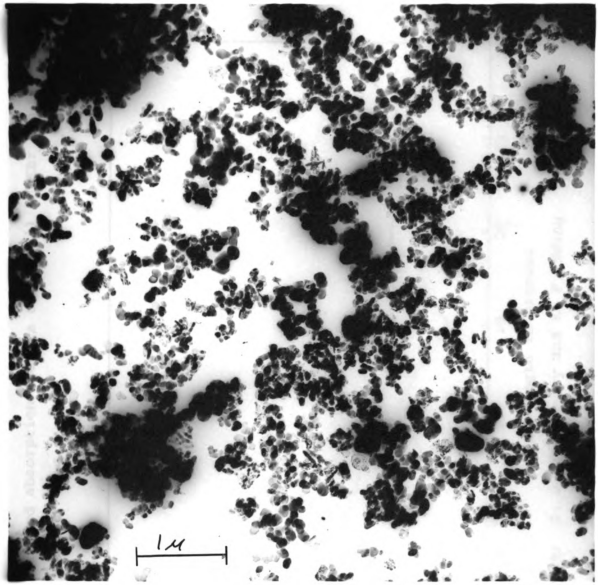

Figure 2.--Electron micrograph of MgO (1). Magnification 23,400 X.

Figure 3.--Infrared absorption spectra of MgO (1) in KBr and CsI pellets.*

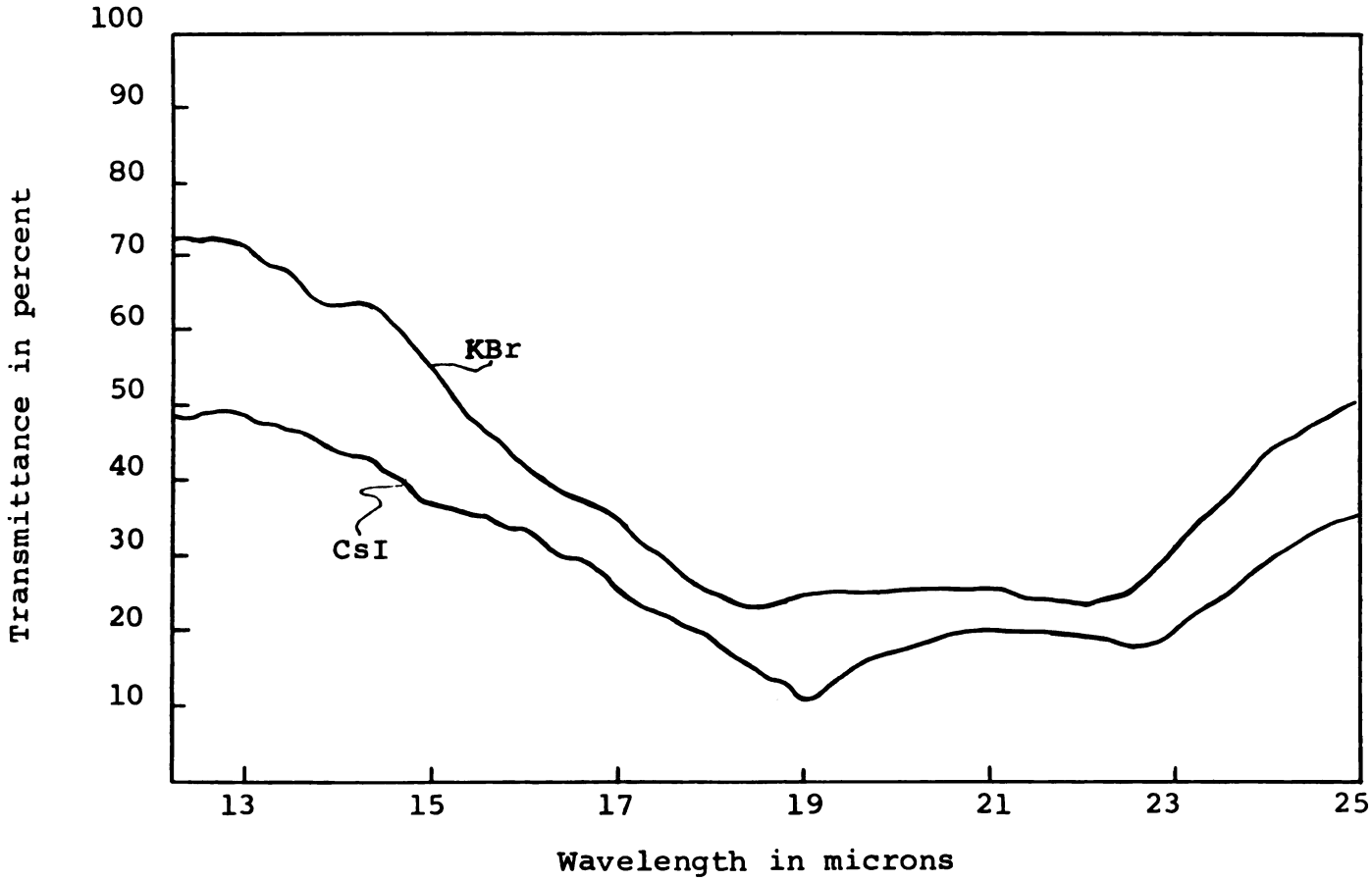

*Source of spectra: D. J. Montgomery and K. F. Yeung.

Figure 4.--Variation of maximum-absorption frequency of MgO (1) with the refractive index of the surrounding medium.

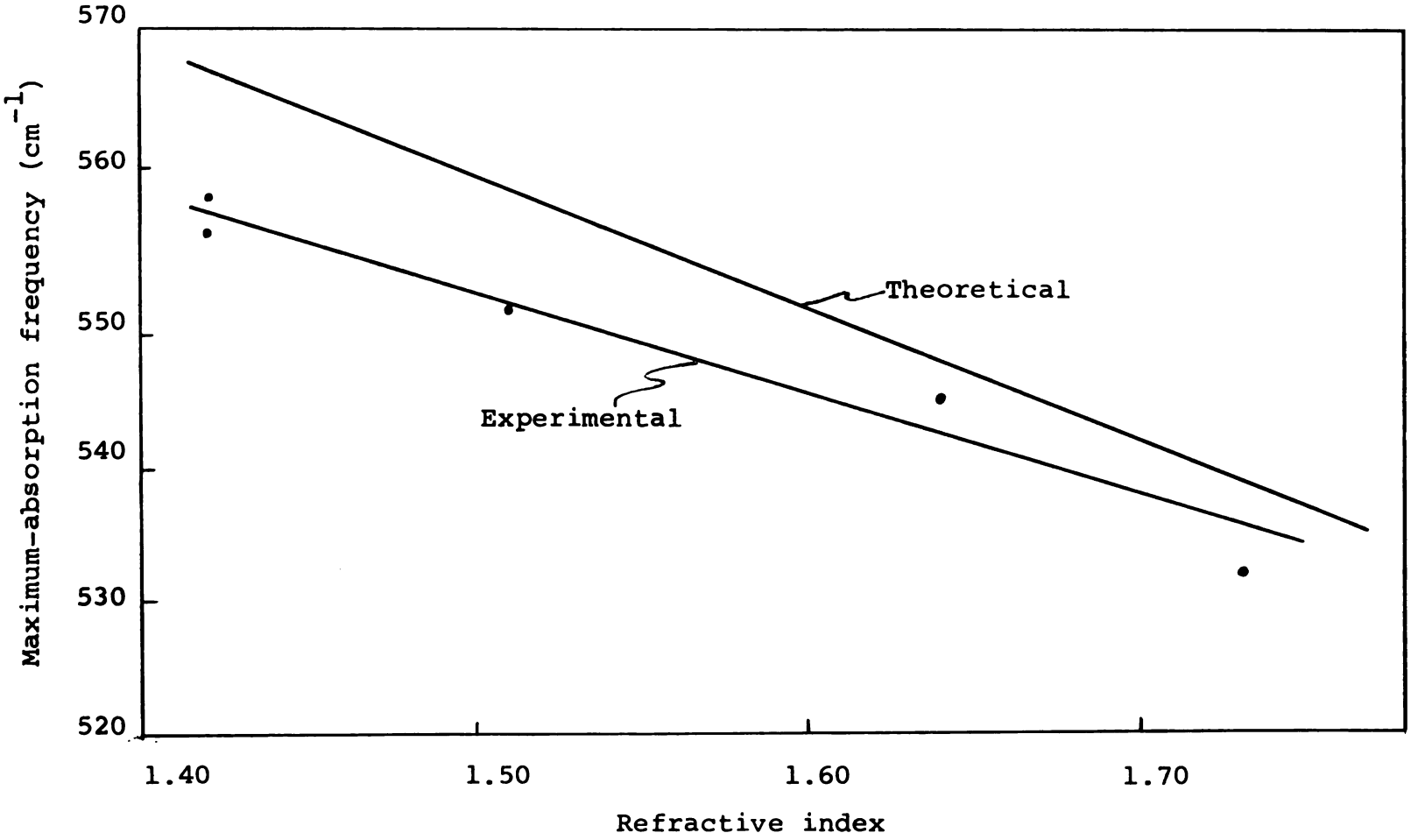

versus refractive index of pellet material for KBr, KCl, NaCl, CsBr, and CsI. The absorption frequencies for each pellet material are averages of the values obtained from several spectra of different pellets.

The second form of MgO, to be referred to as MGO(2), is obtained from burning magnesium ribbon in air to form MgO smoke. An electron micrograph of this smoke deposited directly from the burning ribbon onto a formvar-coated copper grid is given in Fig. 5. The appearance of micrographs of MgO(2), first agitated in water then evaporated onto formvar-coated grids, is essentially the same. The particles appear to be very nearly perfect cubes, except for numerous chain-like particles composed of well-defined cubes stacked in a staggered fashion. Many of the single cubes are 1.5μ or larger on an edge, whereas the chains mostly consist of small cubes, 0.3μ or less, stacked into chains as long as 1.5μ.*

A reproduction of the absorption spectra of MgO(2) fumed directly onto polyethylene plates, and also of the same material dispersed in a Nujol mull is given in Fig. 6.

---

*These thin chains are easily seen on the negative but are not distinct on the print presented in this thesis.

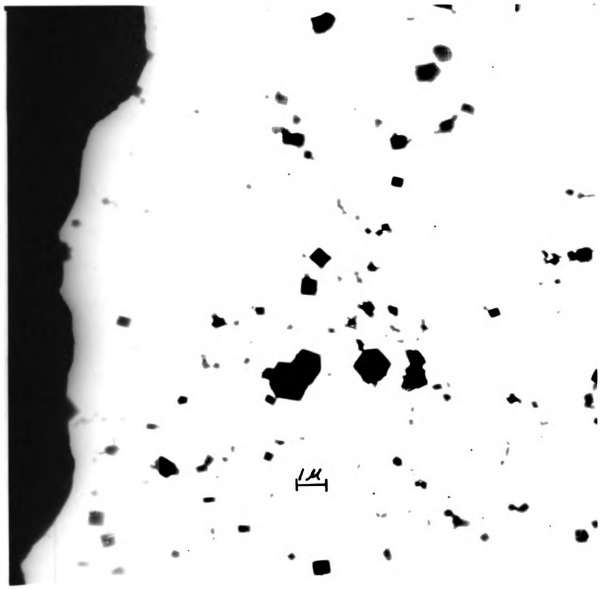

Figure 5.--Electron micrograph of MgO (2) Magnification 7000 X.

Figure 6.--Infrared spectra of MgO (2) fumed on polyethylene -.-.-.-., and dispersed in Nujol --------.

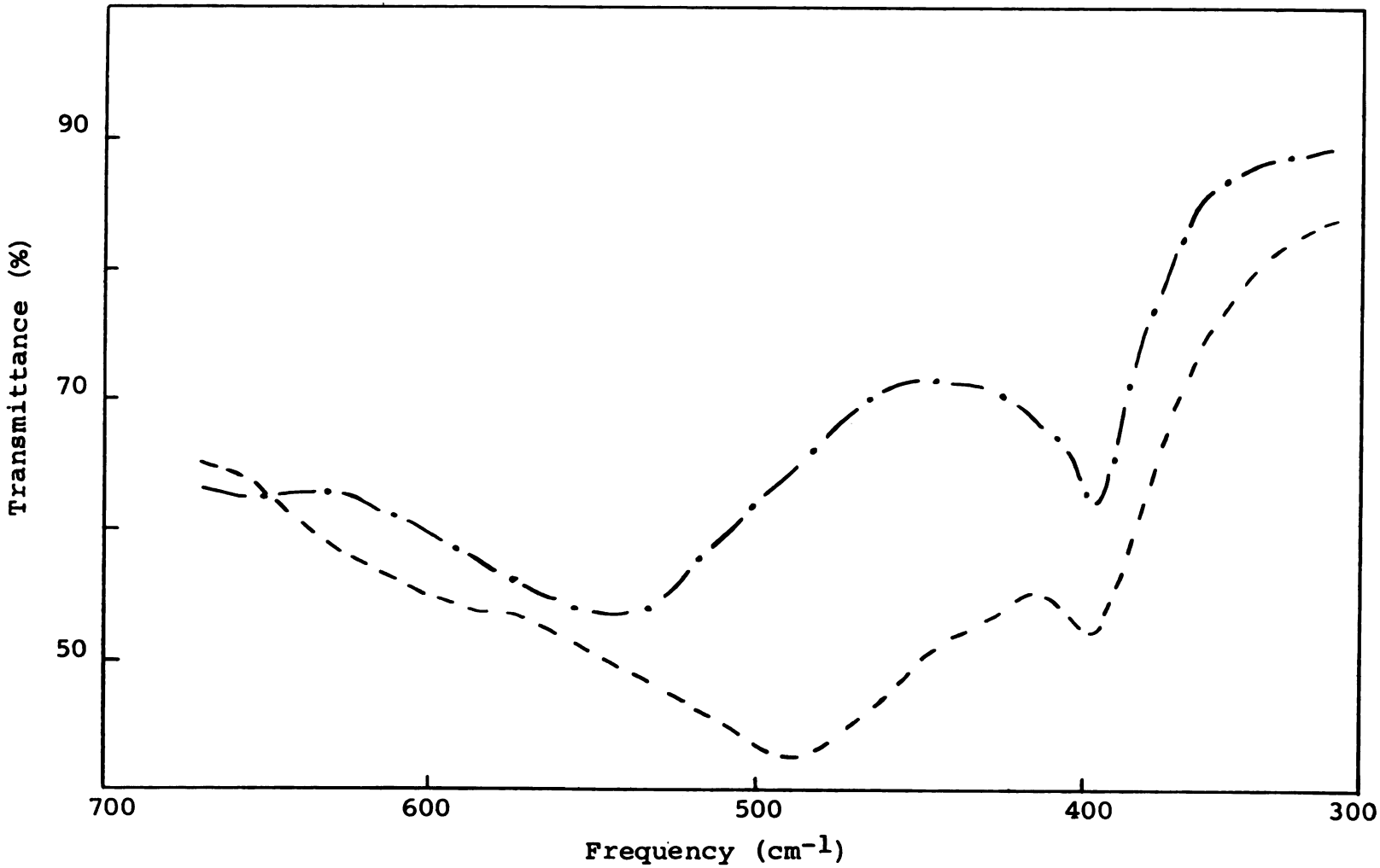

A very strong absorption occurs at 550 cm^{-1} and 488 cm^{-1} respectively, for the MgO(2) fumed onto a polyethylene plate and dispersed in a Nujol mull. Another fairly strong, sharp absorption band occurs near 400 cm^{-1} in both spectra. A weak absorption at 665 cm^{-1} in the spectrum of MgO(2) fumed on polyethylene shifts to 610 cm^{-1} for MgO(2) in Nujol. This value is near the short-wavelength limit of the Perkin-Elmer Model 301 spectrophotometer, and is in a region where polyethylene absorbs strongly and thereby limits the available energy. Nevertheless, the shift of this weak absorption with variation in the medium surrounding the particle is evident in work carried out in Montgomery's laboratory. This work was carried out with KBr plates and KBr pellets, the Perkin-Elmer Model 21 and Perkin-Elmer Model 137 spectrophotometers, whose ranges extend, respectively, to 1000 cm^{-1} and 800 cm^{-1}.

The third form of MgO, to be referred to as MgO(3), is obtained from the thermal decomposition of $MgCO_3$. The grain size of the resulting particles can be controlled by varying the temperature and the duration of heating. Average grain diameters from 50 to 1000 Å are easily obtained. In Table 1 are listed the various average grain sizes that

are obtained by annealing for various combinations of time period and temperature according to Birks and Friedman [25].

TABLE 1.--Grain size in angstroms as a function of annealing time and temperature.

Temperature	Number of Hours					
	2	3	4	6	8	12
400°C	55		60	65		70
600°C	100		110	125		140
800°C	210		240	260		300
900°C		380			500	
1000°C	600			700	800	900

The results shown in Table 1 agree with our electron-microscope findings within a few angstroms for annealing time-temperature combinations of 2 hours at 400°C, 2 hours at 800°C, 3 hours at 800°C, 2 hours at 1000°C. (C.f. Figs. 8, 9.) Hence, we have accepted the values in Table 1 as being reasonably accurate for all the powders which were prepared in this manner for our infrared absorption studies. Optical-microscope and low-magnification electron-microscope observations (Fig. 7) show the MgO(2) particles to be fairly large (up to five microns across), and somewhat platelike.

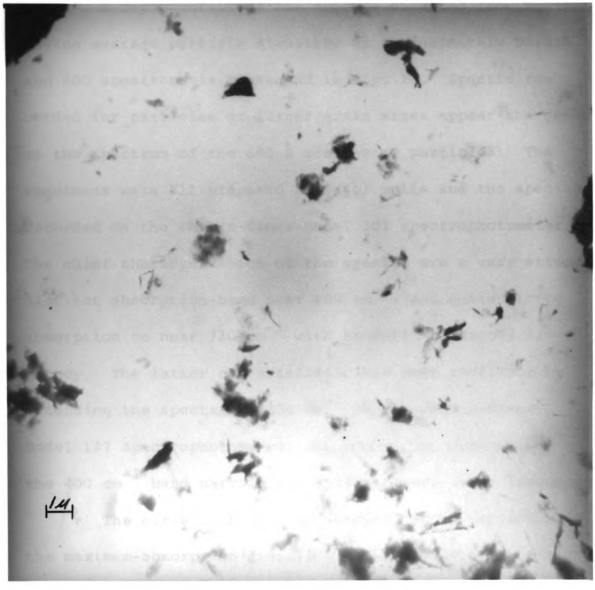

Figure 7.--Electron micrograph of MgO (3). Grain size 60 Å. Magnification 7,000 X.

The higher-magnification micrographs (Figs. 8, 9) reveal the grain structure of these particles.

A reproduction of the spectra obtained from MgO(3) having average particle diameters of approximately 55,210 and 600 angstroms is presented in Fig. 10. Spectra recorded for particles of larger grain sizes appear the same as the spectrum of the 600 Å grain-size particles. The specimens were all prepared in Nujol mulls and the spectra recorded on the Perkin-Elmer Model 301 spectrophotometer. The chief characteristics of the spectra are a very strong, distinct absorption band near 400 cm^{-1}, and quite strong absorption to near 730 cm^{-1} with no definite cutoff frequency. The latter characteristic has been confirmed by extending the spectra to 800 cm^{-1} on the Perkin-Elmer Model 137 spectrophotometer. As grain size increases, the 400 cm^{-1} band narrows and shifts toward lower frequency.

The curve in Figure 11 represents the variation of the maximum-absorption frequency with average grain diameter for grain diameters of 55, 100, 210, 380, 600 and 900 Å. Although relative intensities are difficult to compare, it is apparent that the absorption away from the 400 cm^{-1} band lessens with increasing grain size, and that a distinct

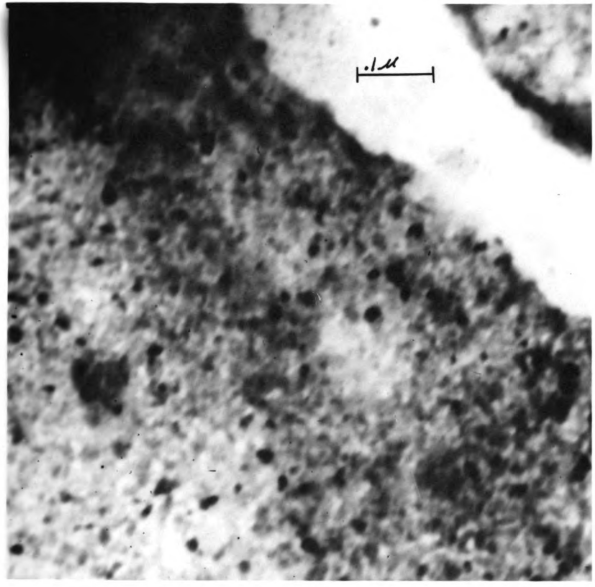

Figure 8.--Electron micrograph of MgO (3). Grain size 100 Å. Magnification 200,000 X.

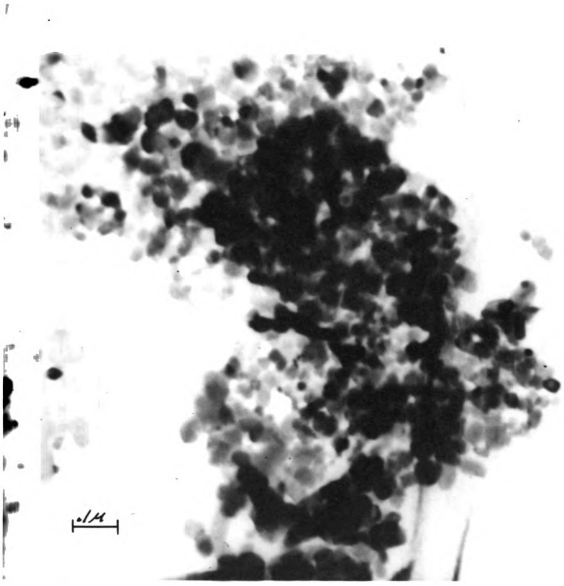

Figure 9.--Electron micrograph of MgO (3). Grain size 600 Å. Magnification 120,000 X.

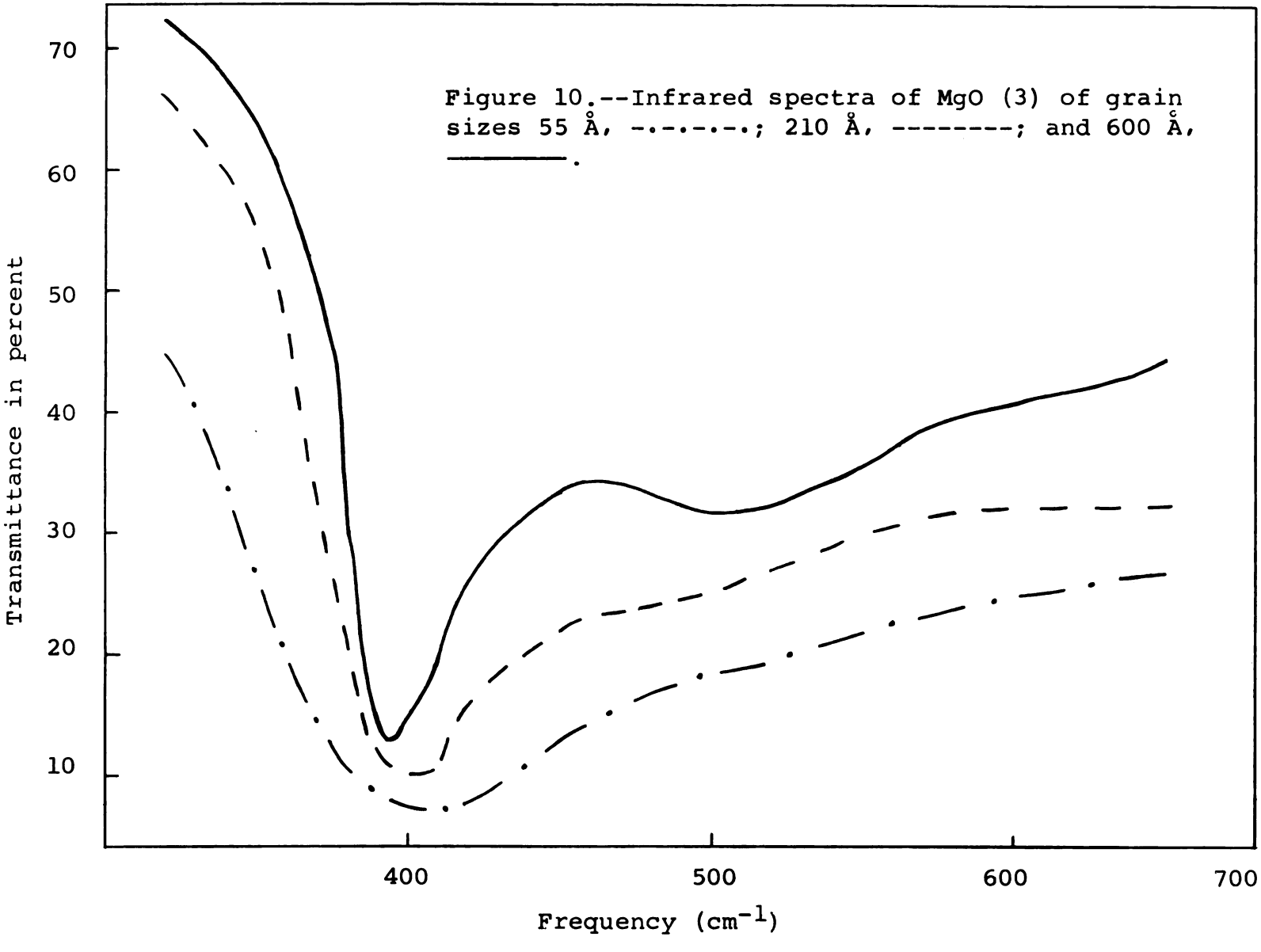

Figure 10.--Infrared spectra of MgO (3) of grain sizes 55 Å, -·-·-·-·-; 210 Å, --------; and 600 Å, ————.

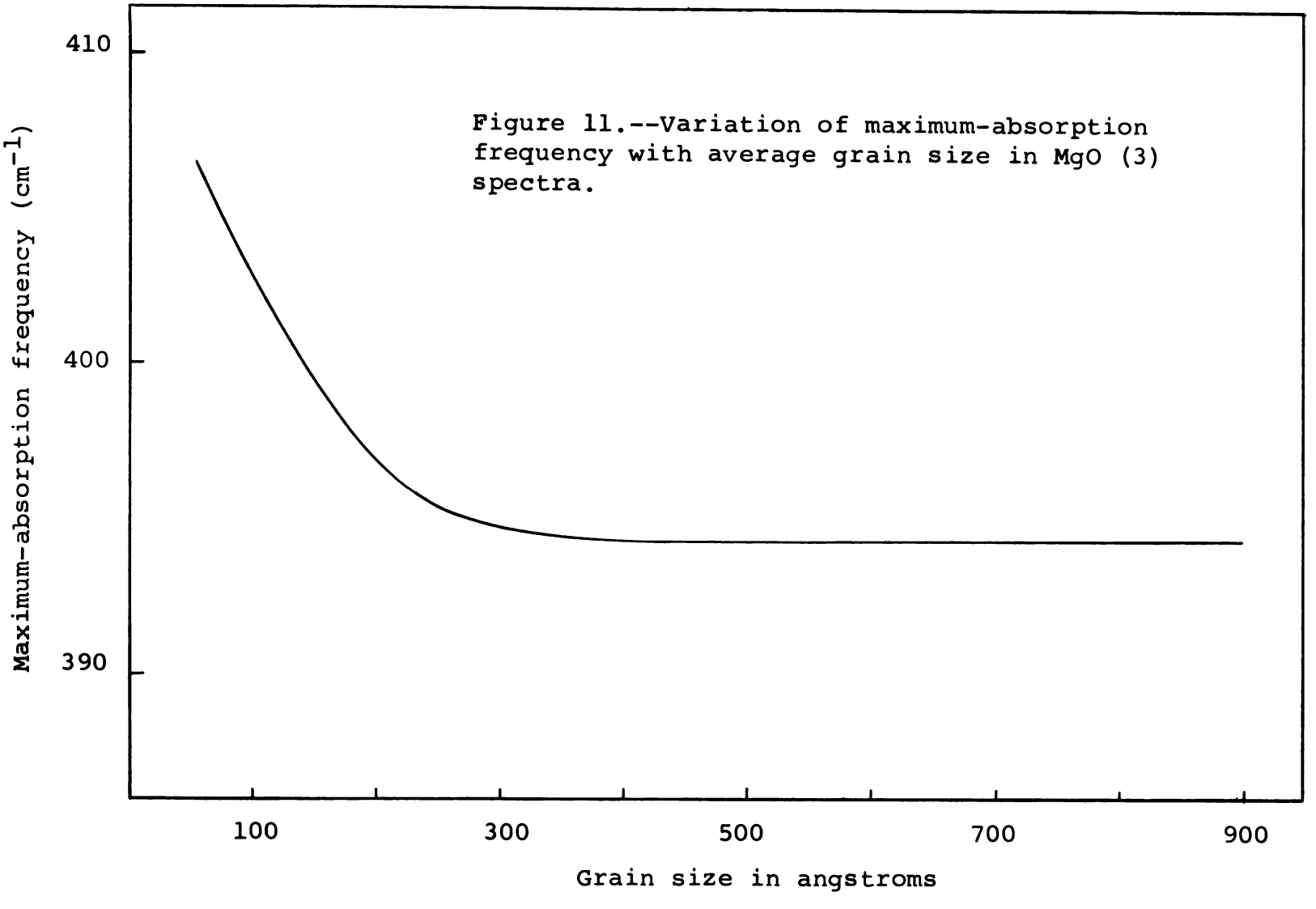

Figure 11.--Variation of maximum-absorption frequency with average grain size in MgO (3) spectra.

absorption band appears at about 500 cm^{-1} with increasing grain size.

There are several significant similarities and differences in the spectra of the three forms of MgO powder. All of the spectra exhibit considerable absorption from roughly 400 cm^{-1} to 730 cm^{-1}. The MgO(2) and MgO(3) spectra have in common a distinct band at approximately 400 cm^{-1}. No such band appears in the MgO(1) spectrum. The MgO(1) and MgO(2) spectra have intermediate bands, i.e., between 500-600 cm^{-1}, and the MgO(3) spectra of larger-grain-size particles apparently begin to develop a distinct band in this region. The MgO(1) and MgO(2) spectra contain distinct, weaker absorptions above the intermediate range (500-600 cm^{-1}) for MgO(2), and below this range for MgO(1). There are no clearly-defined absorptions of this type in the MgO(3) spectra.

B. Rutile (SnO_2 and TiO_2)

Examples of the electron micrographs of SnO_2 and TiO_2 powders are shown respectively in Figs. 12 and 13. Generally the largest dimensions of the particles do not

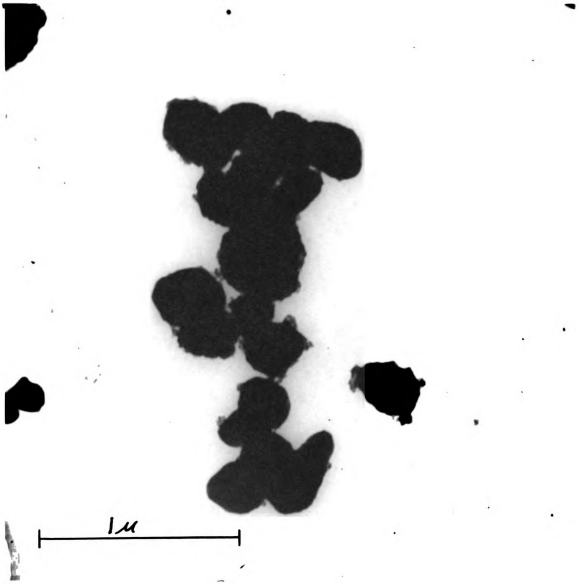

Figure 12.--Electron micrograph of SnO_2. Magnification 54,000 X.

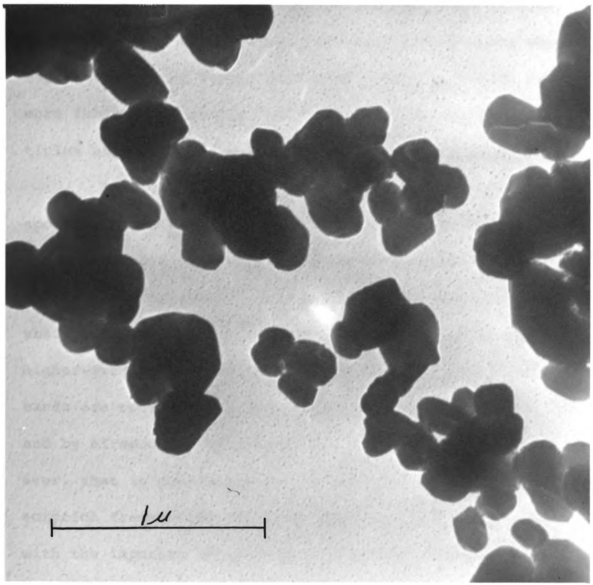

Figure 13.--Electron micrograph of TiO_2. Magnification 58,000 X.

exceed 0.5μ for TiO_2 and 1.5μ for SnO_2. In both powders relatively few particles exceed 0.5μ. The particle shape tends to be rather random, though the particles of both powders tend to exhibit flat faces and fairly sharp edges, especially in the larger particles. SnO_2 particles exhibit more faces per particle, up to twelve, whereas TiO_2 particles seem to have no more than six to eight faces.

In Fig. 14 is given the experimental absorption spectrum of SnO_2 powder as obtained in the present work, and in the work of [26]. These spectra, which are in fairly close agreement, indicate the existence of four absorption bands, with considerable broadening in the higher-frequency regions. Similarly, four absorption bands are obtained for TiO_2 by McDevitt and Baun [27], and by Afremow and Vandeberg [28]. We have found, however, that in contrast with the findings in SnO_2 the absorption frequencies and band shape vary substantially with the impurity content and the method of preparation of the TiO_2 powder. Rutile powders of various impurity content (95% TiO_2 to 99% TiO_2) were studied, and all of our spectra differ in some detail from those of McDevitt and Baun and of Afremow. To some extent the spectra of these investigations disagree with each other. The

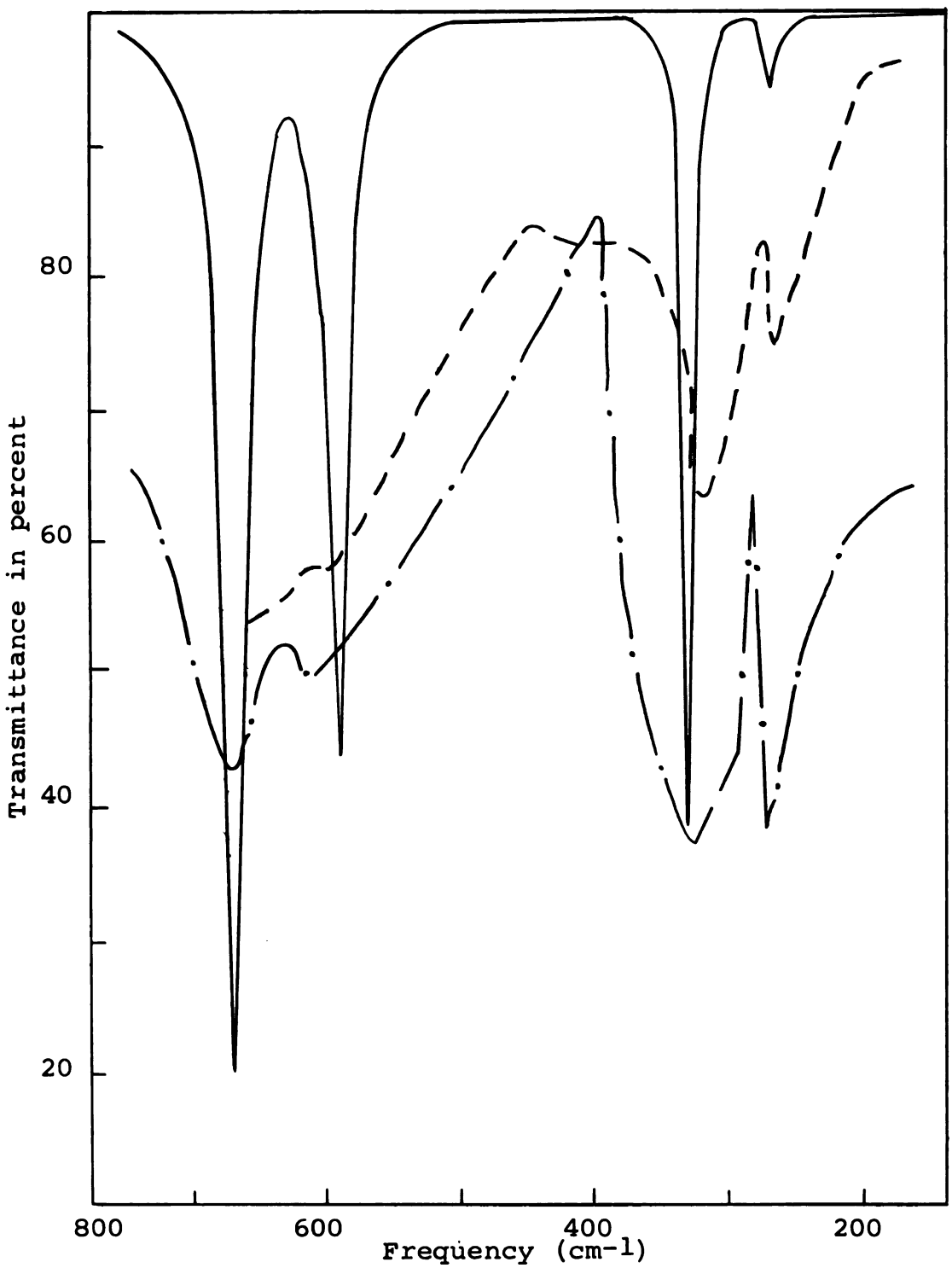

Figure 14.--Experimental and theoretical infrared absorption spectra of SnO_2. McDevitt [26] -.-.-.-.-; ours --------; theoretical ————.

observed frequencies of maximum and minimum absorption for TiO_2 and SnO_2 powders are contained in Table 2.

TABLE 2.--Observed and calculated maximum and minimum infrared-absorption frequencies for SnO_2 and TiO_2 powders.

Material	Frequencies of absorption maxima				Frequencies of absorption minima		
	ν_1	ν_2	ν_3	ν_4			
SnO_2 obs*	670	325	270	610	283	295	635
SnO_2 calc	670	330	270	592	290	310	630
TiO_2 obs+	610	425	350	680	365	460	650
TiO_2 calc	660	440	360	700	400	500	690

*Data due to McDevitt[26]. +Data due to McDevitt & Baun[27].

C. Perovskites ($BaTiO_3$ and $SrTiO_3$)

Electron-microscope observations of $BaTiO_3$ and $SrTiO_3$ (Figs. 15 and 16) indicate that maximum particle dimensions seldom exceed 1.5μ and that the particles tend to have nearly cubic shape, with some of the larger particles exhibiting very flat faces and extremely sharp edges.

Perry, Khanna and Rupprecht [29] recorded the absorption spectrum of $SrTiO_3$ powder from 1 to 1200 cm^{-1}

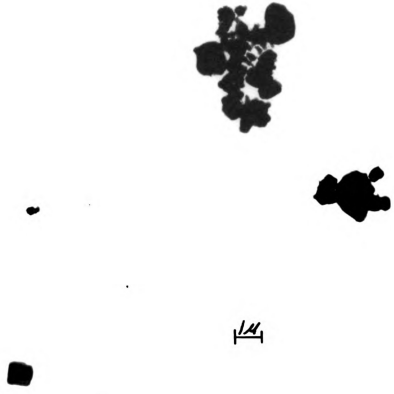

Figure 15.--Electron micrograph of $BaTiO_3$. Magnification 7,000 X.

Figure 16.--Electron micrograph of $SrTiO_3$. Magnification 7,000 X.

(C.f. Fig. 17). They observed three distinct absorption bands. In our laboratory we have verified the essential features of this spectrum in the region 167 to 800 cm^{-1}. Numerous people have recorded the spectrum of $BaTiO_3$, but in the literature we could find no spectra which extended below 300 cm^{-1}. In higher frequency regions, Last [30] and Spitzer et al. [31] found absorptions at 545 and 400 cm^{-1}. We have extended the spectrum of $BaTiO_3$ powder down to 167 cm^{-1}, and thereupon verified the previously mentioned absorptions and revealed a third weak absorption in the neighborhood of 180 cm^{-1}. Figure 17 contains Last's spectrum for $BaTiO_3$ extended to 167 cm^{-1}. In Table 3 are listed the observed absorption frequencies for both $SrTiO_3$ and $BaTiO_3$.

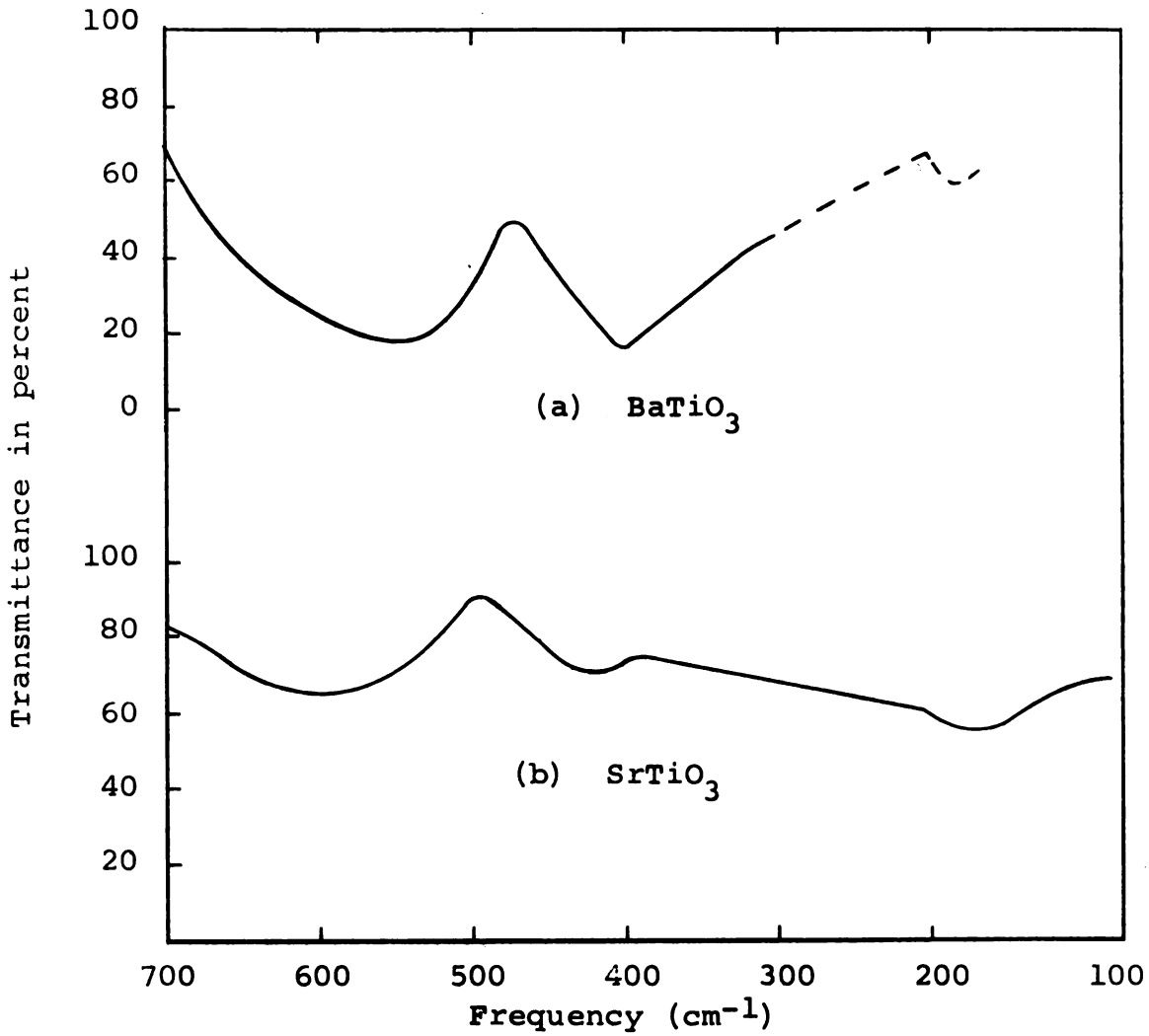

Figure 17.--Infrared absorption spectra of $BaTiO_3$ and $SrTiO_3$.

(a) 700 to 300 cm^{-1}, Last [30]
300 to 167 cm^{-1}, our work

(b) Spectrum due to Perry et al. [29]

TABLE 3.--The TO frequencies determined from single-crystal reflection experiments, together with observed and calculated powder-absorption frequencies for $BaTiO_3$ and $SrTiO_3$ and dielectric constants.

	Single-crystal* TO frequency	Powder+ absorption frequency	Scattering-calculation absorption frequency	Fröhlich-calculation absorption frequency	Dielectric constants††
$BaTiO_3$	510 cm^{-1}	545	600	545 exp.	$\varepsilon_o = 2000$
	183	400	425	400 exp.	$\varepsilon_\infty = 5.2$
	33.8		180	206 predicted	
$SrTiO_3$	546	605	665	605 exp.	$\varepsilon_o = 311$
	178	400	420	400 exp.	$\varepsilon_\infty = 5.3$
	87.5	175	175	200 predicted	

*These values are from Spitzer et al. [31].

+Absorption frequencies for $BaTiO_3$ are due to Last [30], for $SrTiO_3$, to Perry et al. [29].

††Dielectric constant values are from Barker and Hopfield [19].

V. INTERPRETATION OF RESULTS

The major features of the infrared spectra of MgO, SnO_2, TiO_2, $SrTiO_3$, $BaTiO_3$, we submit, can be explained as a consequence of particle shape and particle size. This portion of the thesis is concerned in part with applying the Fröhlich theory and electromagnetic scattering theory to explain the spectra of materials consisting of "small" particles of various shapes. Minor details not accounted for in this manner are attributed to grain-boundary effects, and to the fact that real powder specimens do not adhere strictly to the small-particle assumption. As in the previous section, the discussion will be divided into three parts, viz. one for each crystal structure studied.

A. Magnesium Oxide

In principle, the absorption frequency of powdered MgO may be calculated by either the Fröhlich relation, Eq. 5, for small spheres, or Eq. 41 for other shapes, or alternatively by means of electromagnetic scattering theory.

For small spheres imbedded in a matrix of refractive index 1.5, calculation of the transmittance from Eq. 61 now reduces to $T = 1-NC^{(ext)}$, for MgO which absorbs isotropically. Computation of the complex refractive index of MgO required for the above calcualtion was based on parameters given by Jasperse et al [32], who took a two-oscillator sum to fit the reflectivity data of MgO. The appropriate parameters are listed in Table 4.

TABLE 4.--MgO optical parameters based on the single-crystal-reflection dispersion analysis of Jasperse et al. [32].

Frequency(cm^{-1})		Strength($4\pi\rho$)	Damping γ
υ_{t1}	401	6.60	0.019
υ_{t2}	640	0.45	0.160
	ϵ_∞ =	3.01	ϵ_o = 9.66

The low-strength mode at 640 cm^{-1} required to obtain a good fit to the reflectivity data has little effect on the calculated transmittance, and no effect on the position of the absorption maximum. Equation 5, as well as Eq. 61 yields a value of 550 cm^{-1} for the absorption maximum under the assumption of spheres dispersed in a matrix of refractive

index 1.5. Figure 4 contains plots of frequencies of maximum absorption as obtained experimentally and frequencies of maximum absorption as obtained from Eq. 5 as a function of the refractive index of the surrounding medium. The vertical separation of these curves is 1 to 2%, which is well within the uncertainty in υ_t, the TO frequency. In addition, ϵ_∞ is probably not known to within better than 1 or 2%. Values of ϵ_∞ from 2.95 to 3.05 are found in the literature [32, 33].

We assert that the results illustrated in Fig. 3 establish the nature of the strongest absorption in the MgO (l) spectrum (Fig. 3) as being of the Fröhlich type, i.e. at a frequency predicted by Eq. 5. Further support for this assertion is obtained by an inspection of the electron micrograph of MgO (l), Fig. 2, which shows that a large proportion of the particles do indeed approximate spheres.

The secondary absorption in the MgO (l) spectrum also is observed to shift toward lower frequency with increasing refractive index of the matrix, although no detailed analysis of this shift has been made. A possible explanation of this absorption may be sought in a consideration of the presence of a fairly large incidence of

double particles; axial ratio 2:1. Figure 18 shows plots of maximum absorption frequency versus shape factor g for matrix refractive indices of 1.0 and 1.5 for MgO, as calculated from Eq. 41. If it is assumed that these particles approximate prolate spheroids, the shape factors for polarization parallel and perpendicular respectively to the long axis are $g_{||} = 0.172$ and $g_{\perp} = 0.414$. From Fig. 18, $g_{||} = 0.172$ and n = 1.5 yields an absorption frequency of 450 cm^{-1}, which agrees closely with the experimental value of 460 cm^{-1}. The absorption frequency corresponding to $g_{\perp} = 0.414$ occurs at 540 cm^{-1} which is too close to the spherical-particle absorption of 550 cm^{-1} to be resolved but which contributes to the strength of absorption in this region.

The strongest absorption in the MgO(2) spectrum is interpreted in a fashion similar to the interpretation of the strongest absorption in MgO(1). It is clear, however, that this absorption, which occurs at 546 cm^{-1} for smoke fumed on polyethylene and 490 cm^{-1} for smoke in a Nujol mull, is not due to spherical particles, for these, according to Eq. 5, would absorb at about 605 cm^{-1} when deposited on polyethylene and at 550 cm^{-1} in a Nujol mull. The cubical character of the smoke particles, Fig. 5, leads one to expect absorption at lower frequencies than for spheres.

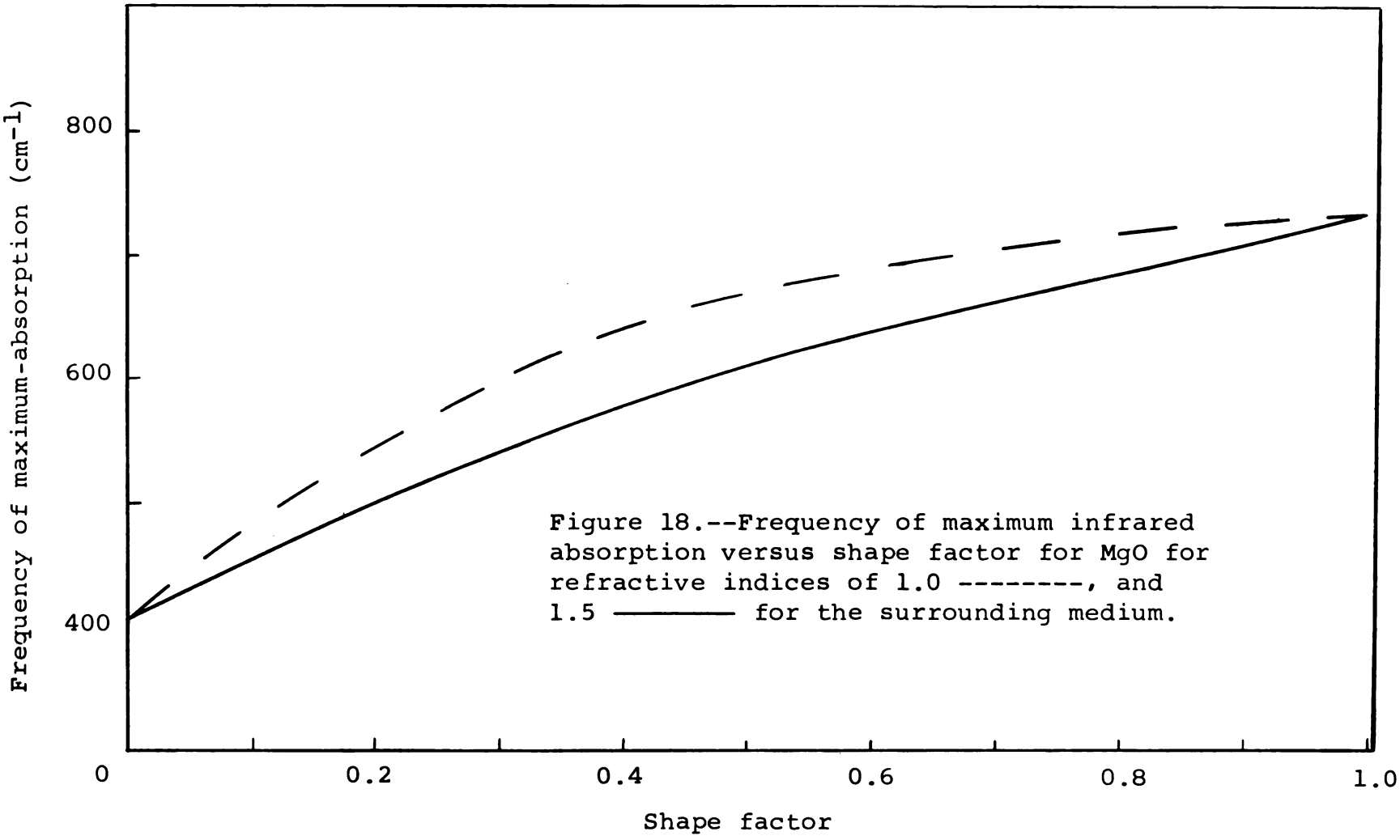

Figure 18.--Frequency of maximum infrared absorption versus shape factor for MgO for refractive indices of 1.0 --------, and 1.5 ———— for the surrounding medium.

This shift is a consequence of the lower overall depolarization effect which gives rise to effective force constants that are less than would be obtained with spheres. No attempt has been made to solve the quite difficult problem of computing the depolarization (shape) factor for cubes. It will be shown that it may be estimated, however, with the aid of Fig. 18. From the curve for a matrix refractive index of 1.0 an absorption frequency of 546 cm^{-1} (observed for MgO smoke fumed on polyethylene) yields a shape factor of 0.21. This shape factor leads to absorption at 500 cm^{-1} for a refractive index of 1.5, according to the lower curve of Fig. 18, in good agreement with 490 cm^{-1} observed for MgO smoke in a Nujol mull. Hence, it is reasonable to conclude that the strongest absorption in the MgO(2) spectrum is of the Fröhlich type, Eq. 41, for cubes, and that the appropriate shape factor for cubes is approximately 0.21.

The weak absorption that appears as a shoulder in the MgO(2) spectrum may also be interpreted as a particle-shape effect. Again from Fig. 18, an absorption at 665 cm^{-1} yields a shape factor of approximately 0.5 for a matrix refractive index of 1.0. This shape factor in turn leads to an absorption at 610 cm^{-1} according to the lower curve of Fig. 18 (matrix refractive index 1.5), which agrees

closely with the value of 607 cm^{-1} obtained for MgO smoke in a Nujol mull. A shape factor of 0.5 corresponds to absorption due to polarization perpendicular to long thin, rod-like particles. Polarization parallel to these rod-like particles would cause absorption at the TO bulk-crystal frequency, which incidendally, is present in this spectrum, although it is not believed that this is the primary cause for absorption at the TO frequency. Such rod-like (or chain-like) particles do occur in the MgO smoke, Fig. 5. The regularity of the stacking of the cubes in these particles indicates that they are single crystals whose growth has followed a characteristic pattern; hence, intimate contact is realized between the stacked cubes along the chain.

The primary cause for the fairly strong, sharp absorption at the TO bulk-crystal absorption frequency ($\sim$ 400 cm^{-1}) is the presence of large MgO cubes for which the small-particle assumption is invalid. The real part of the complex refractive index of MgO is approximately 15.0 at 400 cm^{-1}. This high value produces an internal wavelength of $25\mu/15 = 1.67\mu$ which is comparable with the particle size of the larger particles. A few wavenumbers above 400 cm^{-1} the real part of the MgO refractive index is reduced by at least an order of magnitude, and the small-particle

assumption is again valid. As pointed out previously, the chain or rod-like particles, as well as the large cubes, will absorb at the TO frequency, and neither will exhibit shifts with variation of the refractive index of the surrounding medium (matrix). The sharp low-frequency cutoff of this absorption is consistent with this interpretation, since in the harmonic approximation under no circumstances can the TO frequency lead to absorption below the bulk-crystal value. Furthermore, the half-width of the absorption is comparable with the half-width of the peak in the real part of the complex refractive index 25-30 cm^{-1}, which lends additional credence to the large-particle explanation.

The strong absorption around 400 cm^{-1} in the MgO (3) spectrum (Fig. 11) as in the previous case of MgO (2), results from the presence of particles which are not small compared with the relevant wavelength of radiation, that is, the internal wavelength. As optical microscopy and electron micrographs (Figs. 7, 8, 9) indicate, MgO (3) consists of large flaky particles (a large percentage are several microns across), with a fine-grain structure. Because of the cubic structure of MgO, the grain structure does not alter the general properties with respect to

lattice-vibration absorption. In other words the composite of small grains agglomerated into a single particle behaves optically as a single crystal except for grain-boundary perturbations. The effect of the grain boundaries is manifested both in broadening of the absorption with decreasing grain size (c.f. Figs. 8, 9) and in shift of the absorption frequency to higher frequencies with decreasing grain size (cf. Fig. 10). Although a complete analysis of the grain-boundary effects has not been attempted, some general observations may be made. Both effects correlate closely with the variation in percent of surface atoms of the grains. For a grain size of 55 Å, more than 50% of the atoms are surface or grain-boundary atoms. At a grain size of 380 Å, the percentage of surface atoms is less than 1%. Up to particles with average grain size of 380 Å the variation in line-width and maximum-absorption frequency is appreciable; beyond this grain size, there is no perceptible variation in either of these spectrum properties. Increasing line-width with decreasing particle size is undoubtedly a result, in large part, of the inefficient (irregular) packing in the grain boundaries. An additional effect, particularly with respect to the skewing of the absorption line toward higher frequencies and the resultant

shift in maximum-absorption frequency, arises from the overall shape of the particles (not to be confused with the grains which make up the particles). The fact that the smaller grain-size particles (cf. Fig. 10) exhibit relatively stronger absorption at both the high-frequency limit, the LO bulk-crystal frequency, and at frequencies just above the TO bulk-crystal mode--as well as in between--suggests the presence of particles of highly irregular shapes. As discussed previously this conjecture has been confirmed by the low-magnification electron micrograph Fig. 7 of MgO (3) (approximately 60 Å grain size). The platelet-like particles will absorb near the LO mode for polarization perpendicular to the large surface and near the TO bulk-crystal frequency (on the high side, since the particles are not infinite) for polarization parallel to this surface. Other irregularities in shape will cause absorption at intermediate frequencies. The two extreme cases cited above may be confirmed by substituting the appropriate shape factors into Eq. 41. For E parallel to the large surface, $g \sim 0.0+$, for E perpendicular to the large surface $g = 1.0-$. For other shapes g lies between zero and unity.

It has also been pointed out in Sec. IV that as the average grain size increases, the grains become more clearly defined and begin to separate, that is, strong intimate contact is reduced (Cf. Figs. 8, 9). Consequently, the particles will become less irregular, as sharp edges are more easily knocked off and thin platelet-like particles are broken up in the grinding operation. This interpretation is consistent with the relatively diminishing absorption at the LO and just above the TO bulk-crystal frequencies. It also accounts for the appearance of the distinct intermediate absorption for larger grain sizes. The latter absorption is a result of polarization-induced (Fröhlich type) absorption of the grains themselves acting as independent particles wherever the grain boundaries between individual grains have broken down.

B. Stannic Oxide and Titanium Dioxide (Rutile)

To analyze the absorption spectra of powdered SnO_2 and TiO_2 we first interpret them in terms of the generalized Fröhlich relation, Eq. 41. The particles are assumed to be approximately spherical ($g = 1/3$).

Electron micrographs, Figs. 12, 13, indicate that this assumption is more accurate in the case of SnO_2 than for TiO_2 as discussed in Sec. IV. For the single mode that is active in polarization parallel to the c-axis (E ||c), Eq. 41 becomes:

$$\upsilon_4'/\upsilon_4 = [(\epsilon_{o\,||} + 2\epsilon_m)/(\epsilon_{\infty\,||} + 2\epsilon_m)]^{\frac{1}{2}}. \qquad (68)$$

With the appropriate parameters from Table 5 the frequencies for SnO_2 and TiO_2 are found to be respectively 592 cm^{-1} and 700 cm^{-1}.

TABLE 5.--Oscillator parameters from classical dispersion theory, and dielectric constants of SnO_2 and TiO_2.

	Frequency (cm^{-1})				Strengths			
	υ_1	υ_2	υ_3	υ_4	$4\pi\rho_1$	$4\pi\rho_2$	$4\pi\rho_3$	$4\pi\rho_4$
SnO_2*	605	284	243	465	1.64	1.25	5.8	5.4
TiO_2+	479	386	189	189	2.0	2.2	78.5	165.0

	Damping				Dielectric Constants			
	γ_1	γ_2	γ_3	γ_4	$\epsilon_{o\,\|\|}$	$\epsilon_{o\,\perp}$	$\epsilon_{\infty\,\|\|}$	$\epsilon_{\infty\,\perp}$
SnO_2	0.034	0.022	0.032	0.040	9.6	12.5	4.17	3.78
TiO_2	0.025	0.032	0.101	0.040	173.0	89.0	8.4	6.0

*SnO_2 data due to Summitt [6].

+TiO_2 data due to Spitzer et al. [31].

Referring to the absorption frequencies listed in Table 2, we may see that absorption bands occur at 700 cm^{-1} for TiO_2 and 610 cm^{-1} for SnO_2. We therefore assign these bands to υ_4', thereby identifying the frequencies corresponding to the E||c mode. The remaining three bands then are assigned to the E$\perp$c modes, υ_1', υ_2', and υ_3', without attempting exact identification.

To check this assignment, we write Eq. 41 for E||c again taking g = 1/3 in the spherical approximation:

$$\hat{\upsilon_1}\hat{\upsilon_2}\hat{\upsilon_3}/\upsilon_1\upsilon_2\upsilon_3 = [(\epsilon_{o\perp}+2\epsilon_m)/(\epsilon_{\infty\perp}+2\epsilon_m)]^{\frac{1}{2}} \qquad (69)$$

and substitute appropriate data from the oscillator parameters in Table 5 into this equation. This procedure gives for the left-hand and right-hand sides, respectively, for SnO_2 1.40 and 1.47, and for TiO_2 2.45 and 2.98. The agreement in the case of SnO_2 clearly is better than for TiO_2.

The refractive index n and extinction coefficient k have been calculated as a function of wavelength from the dispersion parameters listed in Table 5 for both SnO_2 and TiO_2. With these values of n and k, $C^{(ext.)}$ was calculated point-by-point as a function of wavelength for E||c and E$\perp$c. Then from Eq. 61 the transmittance may be calculated. The

predicted and experimental frequencies of maximum and minimum absorption are listed in Table 2. The agreement is excellent for SnO_2, but not quite so good for TiO_2. Figure 14 is a plot of the calculated transmittance for SnO_2. The transmittance T has been adjusted so that the maximum absorption of the experimental curve of McDevitt agrees with the theoretical one. Hence, absolute intensities in the plot are meaningless, though a rough estimate of the number of particles in the beam does lead to the correct order of magnitude for T. The relative intensities of the absorption bands in the theoretical curve agree somewhat better with the spectrum of SnO_2 recorded by the writer for substantially lower overall absorption. The better agreement between the experimental and theoretical curves for relatively low absorption may indicate that interaction and multiple-scattering effects alter the relative intensities when the particle density in the mull or pellet is high.

As previously pointed out, $C^{(ext.)}$ may be expanded in a series for greater accuracy. For particles of radius as large as 0.5μ, however, no significant contribution is made by the third and higher term in this series. Moreover, $C^{(sca)}$ is small compared with $C^{(abs)}$; yet it is useful to retain $C^{(sca)}$ in order to determine the form of the

scattering. Its magnitude provides an estimate of the effect of multiple scattering when it is suspected to be present. It turns out, however, that $C^{(abs)}$ and $C^{(sca)}$ both have maxima at the same frequencies. Accordingly, multiple scattering cannot change the positions of the absorption maxima.

As a further check on the consistency of the results we substitute the frequencies of maximum absorption as determined from scattering theory into Eq. 41 for $E \perp c$, and also compare the absorption frequencies for $E \parallel c$ determined by both the Fröhlich and the extinction-cross-section method. For $E \parallel c$ we see that for SnO_2 both methods give 592 cm^{-1}, but for TiO_2 the extinction calculation gives 700 cm^{-1} and Fröhlich's method 705 cm^{-1}. The left-hand and right-hand sides of Eq. 41 with υ_1', υ_2', and υ_3' obtained from the extinction calculation are respectively 1.43 and 1.43 for SnO_2, and 2.98 and 2.98 for TiO_2. It is clear that the two methods are consistent with regard to maximum-absorption frequencies.

On the basis of the success of the calculation of the extinction cross section, it appears that the n and k values determined from single-crystal reflection spectra of SnO_2 and TiO_2 are essentially valid for the powder form

of these crystals, especially SnO_2. As has been pointed out, there is however a lack of correlation for band width, and some disagreement in relative absorption strength. This lack of band shape correlation is true for all materials studied in this work. The observed bands are considerably broader than the calculated ones, and much stronger absorption occurs in some cases than is indicated by the calculation. Because of the accuracy with which absorption frequencies are predicted, it appears likely that the discrepancies do not result from fundamental differences in n and k between the single crystal and the powder, but rather as a consequence of other properties of the particles, including the surface as itself constituting a defect in the periodic structure of the lattice. The disagreement in relative intensities is to some extent a consequence of broadening, but in some cases it is too severe to be explained by that alone. The variation of intensities apparently is a more subtle problem involving the direct effect of finite boundary conditions on lattice-vibration modes, and perhaps multiple scattering and interaction. Deviation from sphericity, such as prolateness and oblateness as we have seen before, will cause shifts in absorption frequency, thus reducing the absorption at the fundamental frequencies and

increasing it elsewhere. A quantitative estimate of the effect of such deviations would require detailed knowledge of crystallographic orientation of the particles as well as of their shape distributions. Such information is neither available nor is it readily obtainable. In addition, defects introduce additional absorption frequencies, thus increasing absorption away from the fundamentals. According to Ruppin and Englman all surface-mode contributions to the extinction cross section are accounted for by the electromagnetic scattering theory. Their finding would seem to make further consideration of surface modes unnecessary unless explicit values of surface-mode frequencies are desired.

The complex refractive index determined from classical dispersion theory is a meaningful physical quantity, and is essentially the same for both single crystal and powder in the case of TiO_2 and SnO_2. This contention is based on the success of extinction theory in predicting absorption frequencies from the complex refractive index, and on the agreement obtained with Eq. 41. The failure to achieve complete agreement between the observed and calculated transmittance versus frequency curves is due

to the inherent nature of the surface of the particles such as shape, and concentration of defects.

C. Barium Titanate and Strontium Titanate

The analysis of $BaTiO_3$ and $SrTiO_3$ powder absorption spectra is basically similar to the analysis of SnO_2 and TiO_2 spectra. Table 3 contains a list of both the theoretical and experimental absorption frequencies for the two perovskites. The theoretical frequencies listed there were determined by the extinction-theory method on the assumption of small spherical particles. The calculated low-frequency mode is in excellent agreement with the experimental low-frequency mode in the case of both $BaTiO_3$ and $SrTiO_3$. The high-frequency modes, however, are 7.0 - 10.0% higher than their experimental counterparts, the highest-frequency mode being shifted the most in each case. This point will be discussed later.

Substitution of the experimental absorption frequencies into the generalized Fröhlich relation with g = 1/3 for spheres (Eq. 41), along with the dispersion parameters listed in Table 3, yields respectively for the left-hand and

right-hand sides 4.97 and 5.7 for $SrTiO_3$, and 11.7 and 14.3 for $BaTiO_3$. The differences are 14% and 18% respectively. On the other hand, use of the calculated frequencies instead of the experimental ones yields 5.8 versus 5.7 for $SrTiO_3$, and 14.6 versus 14.3 for $BaTiO_3$, yielding errors of about 2% in each case. This set of results indicates that the calculated absorption frequencies are consistent with the dielectric constants of the materials. It is asserted, therefore, that the frequency assignments in Table 3 are valid.

Since the electron micrographs of $BaTiO_3$ and $SrTiO_3$, Figs. 15 and 16, indicate some tendency toward the formation of cubical particles, a check of the effect of particle-shape deviations from spherical was made. Figure 19 represents the variation of absorption frequency with shape factor for each of the three modes of $BaTiO_3$ and $SrTiO_3$. Since the shape factor for cubes was deduced to be approximately 0.21 from measurements on MgO, it is reasonable to expect that better agreement for all three modes in the perovskites would be obtained for a shape factor near 0.21. Such indeed is the case, as may be observed from inspection of Fig. 19. For example, a shape factor of 0.24 yields absorption frequencies of 607, 393,

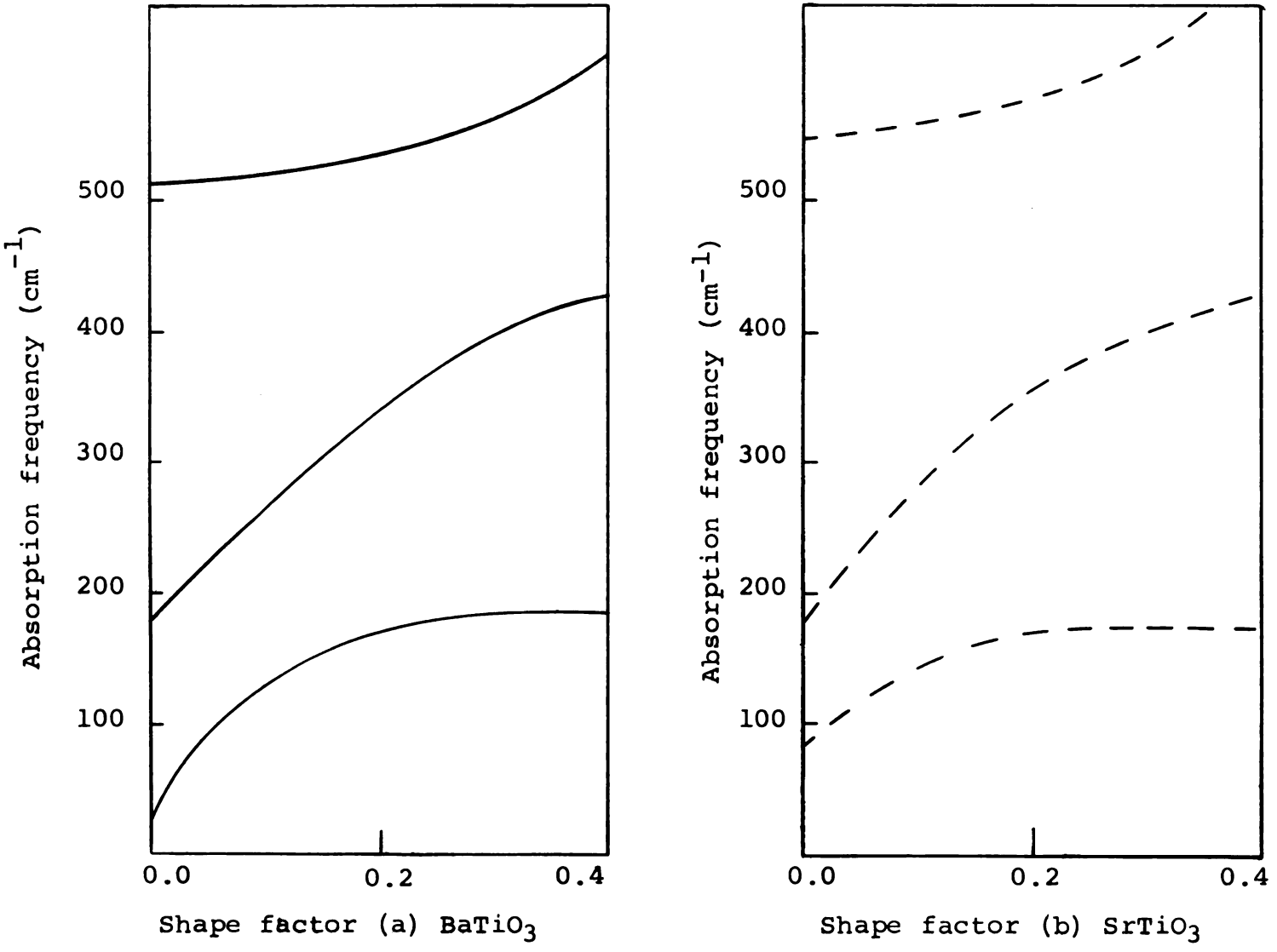

Figure 19.--Variation of the three absorption frequencies of $BaTiO_3$ and $SrTiO_3$ with shape factor.

and 175 cm^{-1} for $SrTiO_3$, and 555, 375, and 180 cm^{-1} for $BaTiO_3$, all of which are in reasonably close agreement with the observed absorption frequencies. It is asserted, therefore, that the absorption spectra of $SrTiO_3$ and $BaTiO_3$ powders are characteristic of "semi-cubical" particles with a shape factor of approximately 0.24.

VI. SUMMARY

In this study we have interpreted the infrared absorption spectra of particulate polar crystalline materials through the use of electromagnetic scattering theory and a generalized Fröhlich relation. This scheme suffices to interpret virtually all of the details of the spectra of the materials studied, which were MgO (cubic, rock salt structure), SnO_2 and TiO_2 (tetragonal rutile structure), and $BaTiO_3$ and $SrTiO_3$ ($SrTiO_3$ is cubic at room temperature, $BaTiO_3$ is slightly distorted cubic or tetragonal structure at room temperature). In the case of MgO three distinct particulate forms were studied, and in all cases the spectral details were found to be consistent with theoretical computations based on size and shape of the particles and refractive index of the medium surrounding the particles. For the rutile and perovskite-structure materials, the shift of the bulk-crystal TO frequencies due to surface polarization is adequately accounted for by scattering theory. These results are consistent with the generalized Fröhlich relation.

Portions of the interpretations presented in Sec. V should not be considered independently, particularly the interpretations of the secondary absorptions in MgO (double particles and long chain-like particles). The overall success, however, of the scattering theory and Fröhlich methods in predicting the positions of the major absorptions lends credence to the interpretations of the secondary absorptions. The inability of the approach taken in this work to obtain a good fit of the theoretical transmittance curves to the experimental transmittance curves, besides predicting the frequencies of maximum absorption, is not unexpected. In all powdered materials the particles may be expected to vary in shape about some average, with some average shape factor g. Variations in shape cause line broadening which would be extremely difficult to take into account quantitatively, and the effort would probably not be justified. Size variations may result in the occurrence of absorptions of both the surface polarization and bulk-crystal type in the same spectrum. We have semi-quantitatively accounted for the effect of shape variation on line width by virtue of the fact that both scattering theory and the Fröhlich relation predict the presence of absorption at frequencies all the

way from the bulk-crystal TO frequencies to the LO frequencies for extreme variations in particle shapes.

The success of our effort to interpret absorption spectra of particulate materials in terms of size and shape makes abundantly clear the danger of reporting absorption spectra of powdered polar materials without taking into account the effects of particle size and shape. On the other hand we have shown that with care such spectra may be interpreted and then used in support of other data. In some cases powder spectra may provide supplementary information when it is not readily available by some other means. For example, when sufficiently large single crystals are not available for low-frequency reflection studies, or in the event that one or more frequencies are too low to measure with available equipment, the polarization-shifted frequency may be measurable.

VII. RECOMMENDATIONS FOR FUTURE WORK

(i) Characterization of various polar crystalline powders according to their average shape factor g, as has been done here in the case of MgO (2), $BaTiO_3$, and $SrTiO_3$. Correlation of these shape factors with optical properties in the visible part of the spectrum would be of interest.

(ii) A detailed theoretical study of the effects of multiple scattering and electromagnetic interaction, although expected to be minor, might clarify some of the discrepancies between the theoretical and observed transmittance curves.

(iii) A thorough experimental study of the effect of particle dispersion within pellets or mulls on the infrared absorption spectrum. This work should be carried out in conjunction with the work suggested in (ii).

(iv) A more complete theoretical investigation of the effect of particle size variation on the infrared

absorption spectrum, particularly in the case of MgO, would provide additional information on the shape of the transmittance curve near the TO mode frequency.

(v) A careful investigation into the exact nature of the variation of absorption frequency with shape factor in crystals with more than one TO mode as in the case of $BaTiO_3$ and $SrTiO_3$ (Sec V). It may be noted in Sec. V, Fig. 19, that the three modes of the perovskites differ substantially in the way in which the variation with shape factor occurs. No physical explanation for this difference has been proffered.

LIST OF REFERENCES

1. M. Born and Th. von Karman, Phys. Zeit. 13, 297 (1912).

2. M. Born and K. Huang, Dynamical Theory of Crystal Lattices, Oxford, Clarendon Press, 1954.

3. D. W. Berreman, Phys. Rev. 130, 2193 (1963).

4. M. Hass, Phys. Rev. Letters. 13, 429 (1964).

5. J. D. Axe and G. D. Pettit, Phys. Rev. 151, 676 (1966).

6. R. Summitt, J. Appl. Phys. 39, 3762 (1968).

7. R. Summitt, Spectrochim. Acta. 23, 2857 (1967).

8. H. Fröhlich, Theory of Dielectrics, Oxford, Clarendon Press, 1958.

9. M. Hass and H. B. Rosenstock, Appl. Optics. 6, 2079 (1967).

10. A. A. Lucas, J. Chem. Phys. 48, 3156 (1968).

11. L. S. Kothari and C. M. Singal, Phys. Rev. 168, 952 (1968).

12. A. A. Lucas, Phys. Rev. 162, 801 (1967).

13. R. Ruppin and R. Englman, J. Phys. C (Proc. Phys. Soc.), 1, 630 (1968).

14. R. Loudon, Adv. Phys. 13, 423 (1964).

15. R. H. Lyddane, R. G. Sachs, and E. Teller, Phys. Rev. 59, 673 (1941).

16. A. S. Barker, Jr., Phys. Rev. 136A, 1290 (1964).

17. W. Ledermann, Proc. Roy. Soc. A182, 362 (1944).

18. J. Van Bladel, Electromagnetic Fields, McGraw-Hill, New York, 1964.

19. A. S. Barker, Jr., and J. J. Hopfield, Phys. Rev. 135, 1732 (1964).

20. H. C. Van de Hulst, Light Scattering by Small Particles, John Wiley and Sons, Inc., New York, 1957.

21. K. S. Yun and G. C. Benson, J. Chem. Phys. 43, 3980 (1965).

22. G. C. Benson, P. I. Freeman, and E. Dempsey, J. Chem. Phys. 39, 302 (1963).

23. M. DiDomenico, Jr., S. H. Wemple, S. P. S. Porto, and R. P. Bauman, Phys. Rev. 174, 522 (1968).

24. P. S. Narayanan, Proc. Indian Acad. Sci. (A) 32, 279 (1950).

25. L. S. Birks, and H. Friedman, J. Appl. Phys. 17, 687 (1946).

26. N. T. McDevitt, private communication.

27. N. T. McDevitt and W. L. Baun, Spectrochim. Acta. 20, 799 (1964).

28. L. C. Afremow and T. T. Vandeberg, J. Paint Tech. 38, 495 (1966).

29. C. H. Perry, B. N. Khanna, and G. Rupprecht, Phys. Rev. 135, A408 (1964).

30. J. T. Last, Phys. Rev. 105, 1740 (1957).

31. W. G. Spitzer, R. C. Miller, D. A. Kleinman, and L. E. Howarth, Phys. Rev. 226, 1710 (1962).

32. J. R. Jasperse, A. Kahan, J. N. Plendl, and S. S. Mitra, Phys. Rev. 146, 526 (1966).

33. A. R. Von Hippel, Editor, Dielectric Materials and Applications, John Wiley and Sons, Inc., New York, 1954.

34. A. S. Barker, Jr., Phys. Rev. 145, 391 (1966).